



Deposited via The University of Sheffield.

White Rose Research Online URL for this paper:

<https://eprints.whiterose.ac.uk/id/eprint/186592/>

Version: Accepted Version

Article:

Colombo, M. and Fairweather, M. (2016) RANS simulation of bubble coalescence and break-up in bubbly two-phase flows. *Chemical Engineering Science*, 146. pp. 207-225. ISSN: 0009-2509

<https://doi.org/10.1016/j.ces.2016.02.034>

© 2016 Elsevier Ltd. This is an author produced version of a paper subsequently published in *Chemical Engineering Science*. Uploaded in accordance with the publisher's self-archiving policy. Article available under the terms of the CC-BY-NC-ND licence (<https://creativecommons.org/licenses/by-nc-nd/4.0/>).

Reuse

This article is distributed under the terms of the Creative Commons Attribution-NonCommercial-NoDerivs (CC BY-NC-ND) licence. This licence only allows you to download this work and share it with others as long as you credit the authors, but you can't change the article in any way or use it commercially. More information and the full terms of the licence here: <https://creativecommons.org/licenses/>

Takedown

If you consider content in White Rose Research Online to be in breach of UK law, please notify us by emailing eprints@whiterose.ac.uk including the URL of the record and the reason for the withdrawal request.

1 **RANS simulation of bubble coalescence and break-up in bubbly two-phase flows**

2

3 **Marco Colombo* and Michael Fairweather**

4 Institute of Particle Science and Engineering, School of Chemical and Process Engineering,
5 University of Leeds, Leeds LS2 9JT, United Kingdom

6 E-mail addresses: M.Colombo@leeds.ac.uk (Marco Colombo); M.Fairweather@leeds.ac.uk
7 (Michael Fairweather)

8 *Corresponding Author: +44 (0) 113 343 2351

9 © 2016. This manuscript version is made available under the CC-BY-NC-ND 4.0 license
10 <http://creativecommons.org/licenses/by-nc-nd/4.0/>
11 Published paper <https://doi.org/10.1016/j.ces.2016.02.034>

12

13 **Abstract**

14

15 In bubbly flows, the bubble size distribution dictates the interfacial area available for the interphase
16 transfer processes and, therefore, understanding the behaviour and the average features of the
17 bubble population is crucial for the prediction of these kinds of flows. In this work, by means of the
18 STAR-CCM+ code, the S_γ population balance model is coupled with an Eulerian-Eulerian two-fluid
19 approach and tested against data on upward bubbly pipe flows. The S_γ model, based on the moments
20 of the bubble size distribution, tracks the evolution of the bubble sizes due to bubble break-up and
21 bubble coalescence. Good accuracy for the average bubble diameter, the velocity and the void
22 fraction radial profiles is achieved with a modified coalescence source. Numerical results show that
23 better predictions are obtained when these flows are considered to be coalescence dominated, but,
24 nevertheless, additional knowledge is required to progress in the development of coalescence and
25 break-up models that include all the possible responsible mechanisms. In this regard, there is a
26 requirement for experimental data that will allow validation of both the predicted bubble diameter
27 distribution and the intensity of the turbulence in the continuous phase which has a significant

28 impact on coalescence and break-up models. An advanced version of the model described, that
29 includes a Reynolds stress turbulence formulation and two groups of bubbles to account for the
30 opposite behaviour of spherical bubbles, which accumulate close to the pipe wall, and cap bubbles,
31 that migrate towards the pipe centre, is proposed. The Reynolds stress model is found to better
32 handle the interactions between the turbulence and the interphase forces, and the use of only two
33 bubble groups seems sufficient to describe the whole bubble spectrum and the bubbly flow regime
34 up to the transition to slug flow.

35

36 **Keywords:** Bubbly flow; RANS modelling; population balance; method of moments; bubble
37 diameter distribution.

38

39

40 **1. Introduction**

41

42 Gas-liquid bubbly flows are common to a variety of processes encountered in numerous industrial
43 sectors, including the nuclear sector as well as chemical and petro-chemical, oil and gas, mining,
44 pharmaceutical and refrigeration industries, amongst others. In the nuclear industry, knowledge of
45 the hydrodynamics of the two-phase flow is essential for the design and operation of boiling water
46 reactors and natural circulation systems, and in the prediction of accident scenarios for pressurized
47 water reactors as well as for other types of reactor. In chemical reactors, such as bubble columns
48 and stirred tanks, gas bubbles are dispersed in the liquid phase to increase phase mixing and
49 enhance heat and mass transfer processes.

50

51 In these flows, the exchange of mass, momentum and energy between the phases depends on the
52 flow conditions, and on the interfacial area concentration in particular. This, in bubbly flows, is
53 determined by the number and the size of the bubbles that are dispersed in the continuous liquid.
54 Often, bubbles are not monodispersed and their distribution is far from steady, and evolves
55 continuously in space and time, following interactions between the bubbles and the continuous
56 phase and collisions between neighbouring bubbles (Lucas et al., 2005; 2010). These interactions
57 induce bubble shrinkage and growth due to the pressure field and bubble break-up and coalescence,
58 and, in boiling or reacting flows, also wall boiling, evaporation and mass transfer. The bubble
59 distribution is therefore governed by these phenomena that, with bubble behaviour strongly related
60 to bubble size and shape (Tomiyama et al., 1998), determine the local flow field, which, at the same
61 time, affect the ratios of mass transfer, break-up and coalescence. In view of this strong coupling,
62 understanding the evolution of the local bubble size distribution in these kinds of flows still
63 represents a rather complex task which, nevertheless, is necessary if we are to be able to predict
64 them with any degree of accuracy.

65

66 The use of computational fluid dynamic (CFD) techniques, applied today in design and as well as a
67 development tool in most of the engineering disciplines, has the potential to significantly improve
68 our ability to predict the mentioned processes. At the present time, application of multiphase CFD
69 to industrial and system-scale calculations has been mainly limited to two-fluid Eulerian-Eulerian,
70 Reynolds-averaged Navier-Stokes (RANS) based models (Prosperetti and Tryggvason, 2009;
71 Tryggvason and Buongiorno, 2010). The use of more advanced techniques, such as direct numerical
72 simulation and large eddy simulation with interface tracking methods (Toutant et al., 2008; Dabiri
73 and Tryggvason, 2015), or Lagrangian tracking techniques (Molin et al., 2012), recently coupled
74 with immersed boundary methods (Santarelli et al., 2015), is mostly constrained to very simple flow
75 conditions in view of the required computational resources (Tryggvason and Buongiorno, 2010).

76

77 In two-fluid Eulerian-Eulerian RANS models, the conservation equations for each phase are derived
78 from averaging procedures. Therefore, the details of the interphase structure are not resolved and
79 interface exchange terms require explicit modelling (Fox, 2012; Prosperetti and Tryggvason, 2009).
80 In these models, the bubble diameter is often needed as an input parameter that, therefore, becomes
81 vital to properly predict the fluid dynamic behaviour of the system. Here, possible limitations can
82 be avoided by coupling the CFD model with the population balance equation (PBE) approach which
83 tracks the behaviour of the bubble size distribution in both physical and internal (e.g. bubble
84 diameter or bubble volume) coordinate spaces (Buffo et al., 2013; Marchisio and Fox, 2005). The
85 use of a PBE combined with CFD has been identified as a crucial development for the accurate
86 prediction of bubbly flows, and significant advances have been achieved in recent years using this
87 approach (Buffo et al., 2013; Cheung et al., 2009, 2013; Lehr et al., 2002; Liao et al., 2015; Lo and
88 Zhang, 2009; Marchisio and Fox, 2005, 2007; Nguyen et al., 2013; Yao and Morel, 2004).

89

90 Many approaches have been considered for the solution of the PBE within a CFD code (Buffo et al.,
91 2013). In class methods, the internal coordinate space, which is usually the bubble size spectrum, is
92 discretized into numerous size classes and the PBE is integrated over each class to give a finite set
93 of discrete PBEs (Kumar and Ramkrishna, 1996; Liao et al., 2015; Lo, 1996; Nandanwar and
94 Kumar, 2008; Wang et al., 2005). In each class, bubbles may be considered as all having the same
95 size (zero-order methods) or a specified distribution (higher-order methods), often a low-order
96 polynomial (Vanni, 2000). In Monte Carlo methods, stochastic differential equations are solved for
97 a finite number of artificial realizations of the dispersed phase population (Lee and Matsoukas,
98 2000; Lin et al., 2002; Zhao et al., 2007). For both the class and Monte Carlo methods, the
99 drawback is the high computational cost involved. Respectively, the solution of at least one
100 conservation equation for each class, with all the relevant source and sink terms, is required, or a
101 very high number of realizations is necessary. In the last two decades, many authors have focused
102 their efforts on the development of the interfacial area transport equation, in the context of both
103 two-fluid CFD models and one-dimensional, advanced thermal hydraulic system codes (Hibiki and
104 Ishii, 2000; Nguyen et al., 2013; Smith et al., 2012; Sun et al., 2004; Wu et al., 1998; Yao and
105 Morel, 2004). Being derived from averaging over the whole bubble diameter spectrum, no bubble
106 size distribution is retained and simplifying assumptions are often made, such as the use of constant
107 or simple linear distributions (Ishii and Hibiki, 2006; Smith et al., 2012). Recently, promising
108 results were achieved with progressively more advanced approaches based on the method of
109 moments, originally introduced by Hulburt and Katz (1964). This method is based on the solution
110 of a set of transport equations for the lower-order moments of the dispersed phase distribution
111 (Marchisio and Fox, 2005). Progressively, more advanced methods have been developed, in
112 particular in the category of quadrature-based methods of moments, such as the direct quadrature
113 method (Marchisio and Fox, 2005) and the conditional quadrature method (Yuan and Fox, 2011).
114 Overall, these methods are reported to provide good predictive accuracy without excessive
115 computational cost (Buffo et al., 2013; Marchisio and Fox, 2005). The S_γ model, proposed by Lo

116 and Rao (2007) for droplet two-phase flows, involves a limited number of moments of the bubble
117 size probability distribution, which is assumed to follow a log-normal shape. The model was later
118 extended to bubbly flows by Lo and Zhang (2009) and its ability to predict with a reasonable
119 accuracy a number of different flows was demonstrated.

120

121 Alongside the method of solution, the other key aspect in regards to population balance based
122 approaches is the availability of reliable closure models for the coalescence and break-up
123 mechanisms. This issue has recently been the subject of numerous researches (Liao et al., 2015; Luo
124 and Svendsen, 1996; Mukin, 2014; Prince and Blanch, 1990; Wang et al., 2005; Yao and Morel,
125 2004), and thorough reviews have been provided by Liao and Lucas (2009) for the break-up
126 mechanism and by Liao and Lucas (2010) for the coalescence mechanism. Despite this, however,
127 commonly accepted and reliable models have not yet emerged in view of the intrinsic complexity
128 encountered when modelling coalescence and break-up in turbulent bubbly flows. Amongst others,
129 the strong mutual interactions with the two-phase turbulence, for which a general and mature model
130 is not yet available, and the coupling and relative importance of the different competitive
131 mechanisms (e.g. turbulent collision, wake entrainment, shearing-off) prevent substantial progresses
132 on the subject being achieved and, therefore, further understanding is required. The ongoing
133 modelling effort is supported by the experimental data available from a number of studies
134 (Grossetete, 1995; Hibiki and Ishii, 1999; Hibiki et al., 2001; Liu, 1993; Lucas et al., 2005, 2010;
135 Prasser et al., 2007; Sanyal et al., 1999). In particular, detailed measurements of the average bubble
136 size and the bubble size distribution have been obtained using the wire-mesh sensor technique
137 (Lucas et al., 2005, 2010; Prasser et al., 2007).

138

139 In this paper, the S_γ model, implemented in the STAR-CCM+ code (CD-adapco, 2014), is combined
140 with an Eulerian-Eulerian two fluid model and tested against data on air-water bubbly flows in
141 pipes. With the aim to improve our ability to predict these flows and the evolution of the bubble

142 diameter distribution, a different coalescence model is introduced and optimized. By means of
 143 sensitivity studies, the relative impact of bubble break-up and coalescence, and the influence of the
 144 continuous phase turbulence and the bubble-induced turbulence, are investigated. In terms of the
 145 turbulent flow field, and in view of the influence it has on the accuracy of the predictions, a
 146 Reynolds stress turbulence model is also included with the aim of extending the model's
 147 applicability to more complex flows, affected by known shortcomings of two-equation turbulence
 148 models. In bubbly flows, which are polydisperse by nature, the size determines the behaviour of the
 149 bubble, with small spherical bubbles flowing near the pipe wall and larger, deformed cap bubbles,
 150 migrating towards the pipe centre (Tomiyama et al., 2002b). Clearly, predicting this behaviour is
 151 mandatory if a general model capable of handling the entire bubble size spectrum is to be
 152 developed. In this regard, two bubble classes, each one with its own behaviour, are introduced in the
 153 final section of the paper. The ability of such a model, limited to only two bubble classes, to predict
 154 the whole bubble spectrum and the transition between wall-peaked and core-peaked void profiles, is
 155 then tested.

156 2. Experimental data

157 For any CFD technique to be applied with confidence, it is mandatory that the model has been
 158 previously validated against relevant experimental data. In this work, seven experiments from Liu
 159 (1993), Hibiki and Ishii (1999), Hibiki et al. (2001) and Lucas et al. (2005) were considered. The
 160 experimental conditions considered are summarized in Table 1.

163 Table 1: Experimental database used for validation.

Case	Source	j_w [m s^{-1}]	j_a [m s^{-1}]	α_{avg} [-]	$d_{B,avg}$ [mm]	Re_L [-]
Hi1	Hibiki et al. (2001)	0.986	0.242	0.191	3.4	49989
Hi2	Hibiki et al. (2001)	2.01	0.471	0.230	3.7	101903
HI1	Hibiki and Ishii (1999)	0.262	0.0549	0.245	3.4	6641
HI2	Hibiki and Ishii (1999)	1.75	0.399	0.253	3.8	44361
L1	Liu (1993)	1.0	0.2	0.160	4.2	57086
L2	Liu (1993)	3.0	0.2	0.062	3.4	171257
Lu1	Lucas et al. (2005)	0.255	0.0368	0.072	-	13030

165

166 Liu (1993) conducted experiments in a vertical pipe of 0.0572 m i.d. to study the bubble diameter
167 and entrance length effects on the void fraction distribution in upward air-water bubbly flows.
168 Bubble velocity, void fraction and average bubble diameter radial profiles were obtained from
169 measurements at different axial locations. Hibiki and Ishii (1999), and Hibiki et al. (2001),
170 measured water and air velocity, turbulence intensity, void fraction, bubble diameter and interfacial
171 area concentration radial profiles at three consecutive axial locations and for an air-water bubbly
172 flows in vertical pipes of diameter 0.0254 m and 0.0508 m. Lucas et al. (2005) used a wire-mesh
173 sensor to study air-water upward flows inside a 0.0512 m diameter pipe. High-resolution
174 measurements of the void fraction and the bubble diameter distribution were obtained. The
175 experiments extended over a wide range of the bubble diameter spectrum, including some mixed
176 radial void profiles where both spherical and cap bubbles were present, one of which was
177 specifically included in the database to validate the model with two bubble classes. Over the whole
178 database, the water superficial velocity considered is in the range $0.262 \text{ m s}^{-1} < j_w < 3.0 \text{ m s}^{-1}$ and
179 the air superficial velocity is in the range $0.0368 \text{ m s}^{-1} < j_a < 0.471 \text{ m s}^{-1}$. Average void fraction α_{avg}
180 and average bubble diameters $d_{B,avg}$ reported in Table 1 were calculated by means of integration of
181 the experimental profiles at the last measurement station. Table 1 also includes values of the
182 Reynolds number of the flows, based on the characteristic dimension along the pipe.

183 184 **3. Mathematical model**

185
186 In a two-fluid Eulerian-Eulerian model, each phase is described by a set of averaged conservation
187 equations. As the cases considered in this paper are limited to adiabatic air-water flows, only the
188 continuity and momentum equations are solved, with the phases treated as incompressible with
189 constant properties:

$$190 \quad \frac{\partial}{\partial t}(\alpha_k \rho_k) + \frac{\partial}{\partial x_i}(\alpha_k \rho_k U_{i,k}) = 0 \quad (1)$$

191

$$\frac{\partial}{\partial t}(\alpha_k \rho_k U_{i,k}) + \frac{\partial}{\partial x_j}(\alpha_k \rho_k U_{i,k} U_{j,k}) = -\alpha_k \frac{\partial}{\partial x_i} p_k + \frac{\partial}{\partial x_j} [\alpha_k (\tau_{ij,k} + \tau_{ij,k}^{Re})] + \alpha_k \rho_k g_i + M_{i,k} \quad (2)$$

192

193 In the above equations, α_k represents the volume fraction of phase k , whereas in the following, only
 194 α will be used to specify the void fraction of air. ρ is the density, \mathbf{U} the velocity, p the pressure and
 195 \mathbf{g} the gravitational acceleration. $\boldsymbol{\tau}$ and $\boldsymbol{\tau}^{Re}$ are the laminar and turbulent stress tensors, respectively,
 196 and M_k accounts for the momentum exchanges between the phases. In the interfacial term, the drag
 197 force, lift force, wall force and turbulent dispersion force are included:

198

$$\mathbf{M}_k = \mathbf{F}_d + \mathbf{F}_l + \mathbf{F}_w + \mathbf{F}_{td} \quad (3)$$

199

200 The drag force represents the resistance opposed to bubble motion relative to the surrounding liquid
 201 and is expressed as:

202

$$\mathbf{F}_d = \frac{3 C_D}{4 d_B} \alpha \rho_c |\mathbf{U}_r| \mathbf{U}_r \quad (4)$$

203

204 Here, \mathbf{U}_r is the relative velocity between the phases and the subscript c identifies the continuous
 205 phase, which is water for all the experiments in Table 1. The drag coefficient, C_D , was calculated
 206 using the model of Tomiyama et al. (2002a), where the effect of the bubble aspect ratio on the drag
 207 was also accounted for (Hosokawa and Tomiyama, 2009) using:

208

$$C_D = \frac{8}{3} \frac{Eo}{E^{2/3}(1 - E^2)^{-1}Eo + 16E^{4/3}} F^{-2} \quad (5)$$

209

210 Here, F is a function of the bubble aspect ratio E . The bubble aspect ratio was derived from the
 211 following correlation and as a function of the distance from the wall y_w (Colombo et al., 2015):

212

$$E = \max \left[1.0 - 0.35 \frac{y_w}{d_B}, E_0 \right] \quad (6)$$

213

214 E_0 is calculated from the expression given by Welleck et al. (1966), where E_0 is the Eötvös number:

215

$$E_0 = \frac{1}{1 + 0.163 E_0^{0.757}} \quad (7)$$

216

217 A lift force, perpendicular to the direction of motion, is experienced by bubbles moving in a shear
218 flow (Auton, 1987), according to:

219

$$\mathbf{F}_l = C_L \alpha \rho_c \mathbf{U}_r \times (\nabla \times \mathbf{U}_c) \quad (8)$$

220

221 In a pipe, the lift force has a strong influence on the radial movement of the bubbles and therefore
222 on the void fraction radial distribution. Generally, a positive value of the lift coefficient C_L
223 characterizes spherical bubbles, which are pushed towards the pipe wall by the lift force. In
224 contrast, larger bubbles, deformed by the inertia of the surrounding liquid, experience a negative lift
225 force and move towards the centre of the pipe (Tomiyama et al., 2002b). In air-water flows, a
226 critical bubble diameter range for the change of sign in the lift coefficient between 5.0 mm and 6.0
227 mm was given by Tomiyama et al. (2002b). These authors also expressed the lift coefficient as a
228 function of the Eötvös number, an approach adopted in other investigations (e.g. Krepper et al.,
229 2008; Rzehak and Krepper, 2013). In this work, however, and in view of previously observed
230 discrepancies between calculations and experimental data when using such an approach, constant
231 values were chosen. More specifically, $C_L = 0.1$ was used for wall-peaked (Lahey and Drew, 2001;
232 Lopez de Bertodano et al., 1994), and $C_L = -0.05$ for core-peaked, void profiles.

233

234 The presence of a solid wall modifies the flow field around the bubbles and the asymmetry in the
 235 flow distribution generates a hydrodynamic pressure difference on the bubble surface that keeps
 236 bubbles away from the wall (Antal et al., 1991):

237

$$\mathbf{F}_w = \max\left(0, C_{w,1} + C_{w,2} \frac{d_B}{y_w}\right) \alpha \rho_c \frac{|\mathbf{U}_r|^2}{d_B} \mathbf{n}_w \quad (9)$$

238

239 In this equation, \mathbf{n}_w is the normal to the wall and C_{w1} and C_{w2} are constants that modulate the
 240 strength and the region of influence of the wall force. Here, values of $C_{w1} = -0.4$ and $C_{w2} = 0.3$ were
 241 used (Colombo et al., 2015). Finally, the turbulent dispersion force was modelled as (Burns et al.,
 242 2004):

243

$$\mathbf{F}_{td} = \frac{3 C_D \alpha \rho_c |\mathbf{U}_r| v_{t,c}}{4 d_B \sigma_\alpha} \left(\frac{1}{\alpha} + \frac{1}{(1-\alpha)} \right) \nabla \alpha \quad (10)$$

244

245 where $v_{t,c}$ is the turbulent kinematic viscosity of the continuous phase, obtained from the turbulent
 246 viscosity $\mu_{t,c}$, calculated from the single-phase relation (more details can be found in the following
 247 Section 3.1, where the turbulence model is presented), divided by the continuous phase density ρ_c .
 248 σ_α is the turbulent Prandtl number for the void fraction, assumed equal to 1.0 (Burns et al., 2004).

249

250 **3.1. Multiphase turbulence modelling**

251

252 Turbulence was solved only in the continuous phase, with a multiphase formulation (CD-adapco,
 253 2014) of the standard k - ε turbulence model (Jones and Launder, 1972):

254

$$\begin{aligned} \frac{\partial}{\partial t} ((1-\alpha)\rho_c k_c) + \frac{\partial}{\partial x_i} ((1-\alpha)\rho_c U_{i,c} k_c) \\ = \frac{\partial}{\partial x_i} \left[(1-\alpha) \left(\mu_c + \frac{\mu_{t,c}}{\sigma_k} \right) \frac{\partial k_c}{\partial x_i} \right] + (1-\alpha) (P_{k,c} - \rho_c \varepsilon_c) + (1-\alpha) S_k^{BI} \end{aligned} \quad (11)$$

255

$$\begin{aligned} & \frac{\partial}{\partial t}((1 - \alpha)\rho_c \varepsilon_c) + \frac{\partial}{\partial x_i}((1 - \alpha)\rho_c U_{i,c} \varepsilon_c) \\ & = \frac{\partial}{\partial x_i} \left[(1 - \alpha) \left(\mu_c + \frac{\mu_{t,c}}{\sigma_\varepsilon} \right) \frac{\partial \varepsilon_c}{\partial x_i} \right] + (1 - \alpha) \frac{\varepsilon_c}{k_c} (C_{\varepsilon,1} P_{k,c} - C_{\varepsilon,2} \rho_c \varepsilon_c) + (1 - \alpha) S_\varepsilon^{BI} \end{aligned} \quad (12)$$

256

257 In the equations above, $P_{k,c}$ is the production term due to shear and S_k^{BI} and S_ε^{BI} the source terms
 258 due to bubble-induced turbulence. The turbulent viscosity $\mu_{t,c}$ was evaluated from the single-phase
 259 relation:

260

$$\mu_{t,c} = C_\mu \rho_c \frac{k_c^2}{\varepsilon_c} \quad (13)$$

261

262 Turbulence was not resolved in the dispersed phase, but was obtained from the continuous phase.
 263 More specifically, it was directly related to the turbulence of the continuous phase by means of a
 264 response coefficient C_t , assumed equal to unity (Gosman et al., 1992; Troshko and Hassan, 2001).
 265 Experimental measurements do in fact suggest that a value of unity is approached starting from void
 266 fractions as small as 6 % (Behzadi et al., 2004).

267

268 In bubbly flows, the generation of turbulence by the bubbles often modifies significantly the
 269 turbulence in the continuous phase, with respect to the single-phase flow (Lance and Bataille, 1991;
 270 Shawkat et al., 2007; Wang et al., 1987). The bubble contribution to turbulence was accounted for
 271 with bubble-induced source terms in Eq. (12) and Eq. (13). In particular, the drag force was
 272 considered as the only source of turbulence generation due to the bubbles and all the energy lost by
 273 the bubbles to drag was assumed to be converted into turbulence kinetic energy inside the bubble
 274 wakes (Kataoka and Serizawa, 1989; Rzehak and Krepper, 2013; Troshko and Hassan, 2001):

275

$$S_k^{BI} = K_{BI} \mathbf{F}_d \mathbf{U}_r \quad (14)$$

276

277 The corresponding turbulence dissipation rate source is equal to the turbulence kinetic energy
 278 source divided by the timescale of the bubble-induced turbulence τ_{BI} . In this work, the mixed
 279 timescale introduced by Rzehak and Krepper (2013) was chosen, derived from the velocity scale of
 280 the turbulence and the length scale of the bubbles:

281

$$S_\varepsilon^{BI} = C_{\varepsilon,BI} \frac{S_k^{BI}}{\tau_{BI}} = 1.0 \frac{k^{0.5}}{d_B} S_k^{BI} \quad (15)$$

282

283 The mixed timescale is expected to mimic the split of eddies which move past the bubbles (Rzehak
 284 and Krepper, 2013) and the shift of the energy of turbulence to smaller length scales observed in
 285 experiments (Lance and Bataille, 1991; Shawkat et al., 2007). The mixed timescale, used in
 286 combination with the coefficient $K_{BI} = 0.25$ in Eq. (14), has been found to provide accurate
 287 predictions over a wide range of bubbly pipe flows (Colombo and Fairweather, 2015).

288

289 A multiphase Reynolds stress turbulence model (RSM) was also included in the overall model and,
 290 based on the single-phase formulation, the Reynolds stresses ($R_{ij} = \tau_{ij}^{Re}/\rho_c$) are given by (CD-
 291 adapco, 2014):

292

$$\begin{aligned} \frac{\partial}{\partial t} \left((1 - \alpha) \rho_c R_{ij} \right) + \frac{\partial}{\partial x_j} \left((1 - \alpha) \rho_c U_{i,c} R_{ij} \right) \\ = \frac{\partial}{\partial x_j} \left[(1 - \alpha) D_{ij} \right] + (1 - \alpha) (P_{ij} + \Phi_{ij} - \varepsilon_{ij}) + (1 - \alpha) S_{ij}^{BI} \end{aligned} \quad (16)$$

293

294 Here, P_{ij} is the turbulence production. The Reynolds stress diffusion D_{ij} was modelled accordingly
 295 to Daly and Harlow (1970), whilst the isotropic hypothesis was used for the turbulence dissipation

296 rate term ε_{ij} . Φ_{ij} is the pressure-strain correlation, accounting for pressure fluctuations that
 297 redistribute the turbulence kinetic energy amongst the Reynolds stress components. This was
 298 modelled using the ‘‘SSG model’’ which is quadratically non-linear in the anisotropy tensor
 299 (Speziale et al., 1991):

300

$$\begin{aligned} \Phi_{ij} = & -[C_{1a}\varepsilon + C_{1b}\text{tr}(P)]a_{ij} + C_2\varepsilon\left(a_{ik}a_{kj} - \frac{1}{3}a_{mn}a_{mn}\delta_{ij}\right) + [C_{3a} - C_{3b}(a_{ij}a_{ij})^{0.5}]kS_{ij} \\ & + C_4k\left(a_{ik}S_{jk} + a_{jk}S_{ik} - \frac{2}{3}a_{mn}S_{mn}\delta_{ij}\right) + C_5(a_{ik}W_{jk} + a_{jk}W_{ik}) \end{aligned} \quad (17)$$

301

302 In Eq. (17), a_{ij} , S_{ij} and W_{ij} are components of the anisotropy, strain rate and rotation rate tensors,
 303 respectively. The bubble-induced turbulence source term was calculated using Eq. (14) and then
 304 split amongst the normal Reynolds stress components following Colombo et al. (2015):

305

$$S_{ij}^{BI} = \begin{bmatrix} 1.0 & 0.0 & 0.0 \\ 0.0 & 0.5 & 0.0 \\ 0.0 & 0.0 & 0.5 \end{bmatrix} S_k^{BI} \quad (18)$$

306

307 Values of the coefficients used for the k - ε model and the RSM can be found in Table 2.

308

309

Table 2. Coefficients of the turbulence models.

k - ε	$\sigma_k = 1.0$; $\sigma_\varepsilon = 1.3$; $C_{1\varepsilon} = 1.44$; $C_{2\varepsilon} = 1.92$; $C_\mu = 0.09$
RSM SSG	$C_{1a} = 1.7$; $C_{1b} = 0.9$; $C_2 = 1.05$; $C_{3a} = 0.8$; $C_{3b} = 0.65$; $C_4 = 0.625$; $C_5 = 0.2$

310

311

312 3.2. The S_γ model

313

314 The S_γ model (Lo and Rao, 2007; Lo and Zhang, 2009) was used to model the evolution of the
 315 bubble population following break-up and coalescence events. In the S_γ model, the bubble size
 316 distribution is assumed to obey to a pre-defined log-normal probability distribution $P(d_B)$.

317 Therefore, it is not necessary to divide the bubble size spectrum into a large number of bubble

318 classes, but the bubble population can be characterized from a limited number of parameters, S_γ ,
 319 related to the moments of the bubble size distribution M_γ :

320

$$S_\gamma = nM_\gamma = n \int_0^\infty d_B^\gamma P(d_B) d(d_B) \quad (19)$$

321

322 where n is the bubble number density. The zeroth order moment is equal to the bubble number
 323 density n , whereas S_2 and S_3 are closely related to the interfacial area concentration a_i and to the
 324 void fraction:

325

$$S_0 = n; S_2 = n \int_0^\infty d_B^2 P(d_B) d(d_B) = \frac{a_i}{\pi}; S_3 = n \int_0^\infty d_B^3 P(d_B) d(d_B) = \frac{6\alpha}{\pi} \quad (20)$$

326

327 From a knowledge of S_2 and S_3 , the average bubble diameter can be determined by using the
 328 definition of the Sauter mean diameter (SMD):

329

$$d_{SM} = d_{32} = \frac{S_3}{S_2} = \frac{6\alpha}{a_i} \quad (21)$$

330

331 In addition, the variance of the distribution can also be calculated:

332

$$\sigma^2 = \ln\left(\frac{d_{32}}{d_{30}}\right) = \ln\left[\frac{(S_3/S_2)}{(S_3/S_0)^{1/3}}\right] \quad (22)$$

333

334 The two average diameters, d_{32} and d_{30} , are equal only in presence of a homogeneous distribution.

335 Once the model is combined with a two-fluid Eulerian–Eulerian model that solves for the void

336 fraction, S_3 is known, and only two additional moments, namely S_0 and S_2 , are sufficient to

337 characterize the bubble size distribution. For each moment, a transport equation of the following
 338 type needs to be solved:

339

$$\frac{\partial S_\gamma}{\partial t} + \nabla \cdot (S_\gamma \mathbf{U}_a) = S_{br}^\gamma + S_{cl}^\gamma \quad (23)$$

340

341 In this equation, the velocity of the air \mathbf{U}_a is given by the two-fluid model and S_{br}^γ and S_{cl}^γ are
 342 source terms that account for bubble break-up and coalescence in the γ^{th} moment equation. Amongst
 343 the different mechanisms, interactions induced by turbulence were assumed to be dominant (Lo and
 344 Zhang, 2009; Yao and Morel, 2004) and the only sources of break-up and coalescence in Eq. (23).

345

346 The source term for bubble break-up is expressed as:

347

$$S_{br}^\gamma = \int_0^\infty K_{br} \Delta S_\gamma^{br} n P(d_B) d(d_B) \quad (24)$$

348

349 Here, K_{br} is the break-up rate, which is the reciprocal of the break-up time τ_{br} . ΔS_γ^{br} is the change in
 350 S_γ due to a single break-up event, which, from conservation of volume, is:

351

$$\Delta S_\gamma^{br} = d_B^\gamma \left(N_f^{\frac{3-\gamma}{3}} - 1 \right) \quad (25)$$

352

353 The number of daughter bubbles N_f was assumed equal to 2 (Lo and Zhang, 2009; Luo and
 354 Svendsen, 1996; Yao and Morel, 2004). The break-up source term then becomes:

355

$$S_{br}^\gamma = \int_0^\infty \frac{d_B^\gamma \left(N_f^{\frac{3-\gamma}{3}} - 1 \right)}{\tau_{br}} n P(d_B) d(d_B) \quad (26)$$

356

357 The break-up timescale follows from the frequency of the second oscillation mode of a droplet (Lo
358 and Zhang, 2009):

359

$$\tau_{br} = 2\pi k_{br} \sqrt{\frac{3\rho_d + 2\rho_c}{192\sigma}} d_B^3 \quad (27)$$

360

361 where $k_{br}=0.2$, the subscript d identifies the dispersed phase and σ is the surface tension. The break-
362 up criterion was expressed as a function of a critical Weber number We_{cr} , therefore a bubble breaks
363 when the Weber number is higher than the critical value:

364

$$d_{cr} = (1 + C_\alpha) \left(\frac{2\sigma We_{cr}}{\rho_c} \right)^{3/5} \varepsilon^{-2/5} \quad (28)$$

365

366 C_α , equal to 4.6, is a correction factor that accounts for nearby bubbles that disrupt the influence of
367 the surrounding inertial forces. In Lo and Zhang (2009), $We_{cr} = 0.31$, whilst in Yao and Morel
368 (2004), $We_{cr} = 1.24$.

369

370 The general source term for bubble coalescence is:

371

$$S_{cl}^Y = \int_0^\infty \int_0^\infty K_{cl}^{d,d'} \Delta S_{\gamma,cl}^{d_B,d'_B} n^2 P(d'_B) d(d'_B) P(d_B) d(d_B) \quad (29)$$

372

373 Here, $K_{cl}^{d,d'}$ is the coalescence rate between two bubbles with diameters d_B and d_B' , and $\Delta S_{\gamma,cl}^{d_B,d'_B}$ is
374 the change in S_γ due to a single coalescence event. To avoid excessive complication, a uniform

375 bubble distribution with an equivalent mean diameter d_{eq} was assumed when computing the change
376 in S_γ due to a single coalescence event (Lo and Zhang, 2009):

377

$$\Delta S_{\gamma,cl}^{d,d'} = d_{eq}^\gamma (2^{\gamma/3} - 2) \quad (30)$$

378

379 The coalescence rate is expressed as:

380

$$K_{cl}^{d,d'} = F_{cl} k_{cl} d_{eq}^2 u_r P_{cl} \quad (31)$$

381

382 Following Chester (1991), Lo and Zhang (2009) considered two different coalescence mechanisms
383 resulting from viscous and inertial collisions. For viscous coalescence, the film drainage model was
384 applied for the coalescence probability (Prince and Blanch, 1990). When two bubbles collide, they
385 trap a thin liquid film between them that prevents coalescence. If the interaction time in the
386 turbulent flow is sufficient for the film to drain out until rupture of the film occurs, then the bubbles
387 coalesce, otherwise the bubbles are separated and coalescence does not occur. The drainage time
388 was calculated from a model for a partially mobile interface and a quasi-steady flow in the film (Lo
389 and Zhang, 2009):

390

$$t_d = \frac{\pi \mu_d \sqrt{F_i}}{2 h_{cr}} \left(\frac{d_{eq}}{4 \pi \sigma} \right) \quad (32)$$

391

392 Here, F_i is the interaction force during collision and h_{cr} the critical film thickness (Lo and Zhang,
393 2009). The coalescence probability is then expressed from the interaction time t_i and the drainage
394 time t_d :

395

$$P_{cl} = \exp(-t_d/t_i) = \exp(t_d\dot{\gamma}) \quad (33)$$

396
397 where the interaction time is the inverse of the Kolmogorov shear rate:

$$\dot{\gamma} = \sqrt{\frac{\varepsilon\rho_c}{\mu_c}} \quad (34)$$

399
400 Finally, in Eq. (31), $k_{cl} = (8\pi/3)^{0.5}$ and the relative velocity between the bubbles $u_r = \dot{\gamma}d_{eq}$.
401 Alternatively, for inertial collision, $k_{cl} = (2\pi/15)^{0.5}$ and $u_r = (\varepsilon d_{eq})^{1/3}$. With regard to the probability
402 of coalescence, the major role is played by bubble shape oscillations and, therefore, the coalescence
403 probability was expressed following Chester (1988):

$$P_{cl} = \frac{\Phi_{max}}{\pi} \left[1 - \frac{k_{cl,2}^2 (We - We_0)^2}{\Phi_{max}^2} \right]^{1/2} \quad (35)$$

405
406 where Φ_{max} is the maximum phase difference (Lo and Zhang, 2009), $k_{cl,2} = 12.7$, $We_0 = 0.8We_{cr}$ and
407 $h_0 = 8.3h_{cr}$.

408
409 A different coalescence model, proposed by Yao and Morel (2004), was also considered in this
410 work. When using the Yao and Morel (2004) approach, the break-up model described above was
411 retained, except for the value of We_{crit} which was modified to 1.24, following the authors' proposal.
412 In Yao and Morel (2004), the number of coalescence events per unit volume and unit time, which is
413 assumed to be mainly due to the collisions induced by turbulence, is expressed as:

$$K_{cl}^{d,d'} n^2 = -C_1 \frac{\varepsilon^{1/3} \alpha^2}{d_{SM}^{11/3}} \frac{1}{g(\alpha) + C_2 \sqrt{We/We_{crit}}} \exp\left(-C_3 \sqrt{We/We_{crit}}\right) \quad (36)$$

415

416 The first part of this equation represents the collision rate between the bubbles, whilst the
417 exponential function describes the probability of coalescence following a collision event. The
418 function $g(\alpha)$ accounts for the effect of the packing of the bubbles when the void fraction is higher
419 than a certain value. From Yao and Morel (2004), $C_1 = 2.86$, $C_2 = 1.922$, $C_3 = 1.017$ and $We_{crit} =$
420 1.24.

421

422 When two groups of bubbles were included, additional source terms were added to the mass and
423 momentum conservation equations to account for the exchanges between the groups. In a similar
424 manner as above, the conservation equation for the moment of the bubble size distribution becomes:

425

$$\frac{\partial S_{\gamma,n}}{\partial t} + \nabla \cdot (S_{\gamma,n} \mathbf{U}_{a,n}) = S_{br,n}^{\gamma} + S_{cl,n}^{\gamma} + D_{br,n}^{\gamma} + B_{cl,n}^{\gamma} + B_{br,n}^{\gamma} + D_{cl,n}^{\gamma} \quad (37)$$

426

427 In this equation, the subscript n identifies the bubble group and assumes the values s for spherical
428 bubbles and c for cap bubbles. D_{br}^{γ} and D_{cl}^{γ} are source terms for the death of bubbles by break-up to
429 the previous group and by coalescence to the following group. Conversely, B_{br}^{γ} and B_{cl}^{γ} are due to
430 the birth of bubbles by coalescence from the previous group and by break-up from the following
431 group. Obviously, when only two groups are considered, Eq. (37) simplifies and the only source
432 terms to be considered are the death of cap bubbles which gives rise to the birth of spherical bubbles
433 by break-up, and the death of spherical bubbles with the birth of cap bubbles by coalescence.

434

435 In this work, break-up of cap bubbles into spherical bubbles has been neglected, with this
436 assumption explained and justified in detail in the results section. To calculate the additional
437 sources accounting for exchanges between groups, using Eq. (29), Eq. (30) and the hypothesis of a

438 uniform bubble distribution for the coalescence source, the source terms for the death of spherical
 439 bubbles by coalescence are obtained as:

440

$$D_{cl,s}^0 = -2 \cdot (K_{cl,s}^{d,d'} n_s^2) f(d_B) \quad (38)$$

441

$$D_{cl,s}^2 = -2d_{eq}^2 (K_{cl,s}^{d,d'} n_s^2) f(d_B) \quad (39)$$

442

443 $f(d_B)$ is a function that expresses the probability that a coalescence event between two spherical
 444 bubbles leads to the birth of a cap bubble. Therefore, it is the ratio of the number of coalescence
 445 events that generate a cap bubble to the total number of coalescence events amongst the spherical
 446 bubble population. The coefficients -2 and $-2d_{eq}^2$ are calculated from the second contribution to Eq.
 447 (30) and reflect the fact that, in these events, the results is not a net change in the value of S_γ for the
 448 spherical bubbles, but a loss of two bubbles and their interfacial area to the cap bubbles.
 449 Accordingly, from the first contribution to Eq. (30), the gain in S_γ in the cap bubble group due to
 450 coalescence events in the spherical bubble group is obtained as:

451

$$B_{cl,c}^0 = (K_{cl,c}^{d,d'} n_c^2) f(d_B) \quad (40)$$

452

$$B_{cl,c}^2 = 1.59 \cdot d_{eq}^2 (K_{cl,c}^{d,d'} n_c^2) f(d_B) \quad (41)$$

453

454 From Eq. (38), the mass source from spherical to cap bubbles can be obtained, using the volume
 455 average bubble diameter:

456

$$\Gamma_{sc} = -\Gamma_{cs} = -D_{cl,s}^0 \frac{\pi d_{30,s}^3}{6} \rho_a \quad (42)$$

457

458 Finally, for simplicity, the function $f(d_B)$ was assumed equal to ratio of the SMD to the critical
459 diameter:

460

$$f(d_B) = \frac{d_{SM}}{d_c} \quad (43)$$

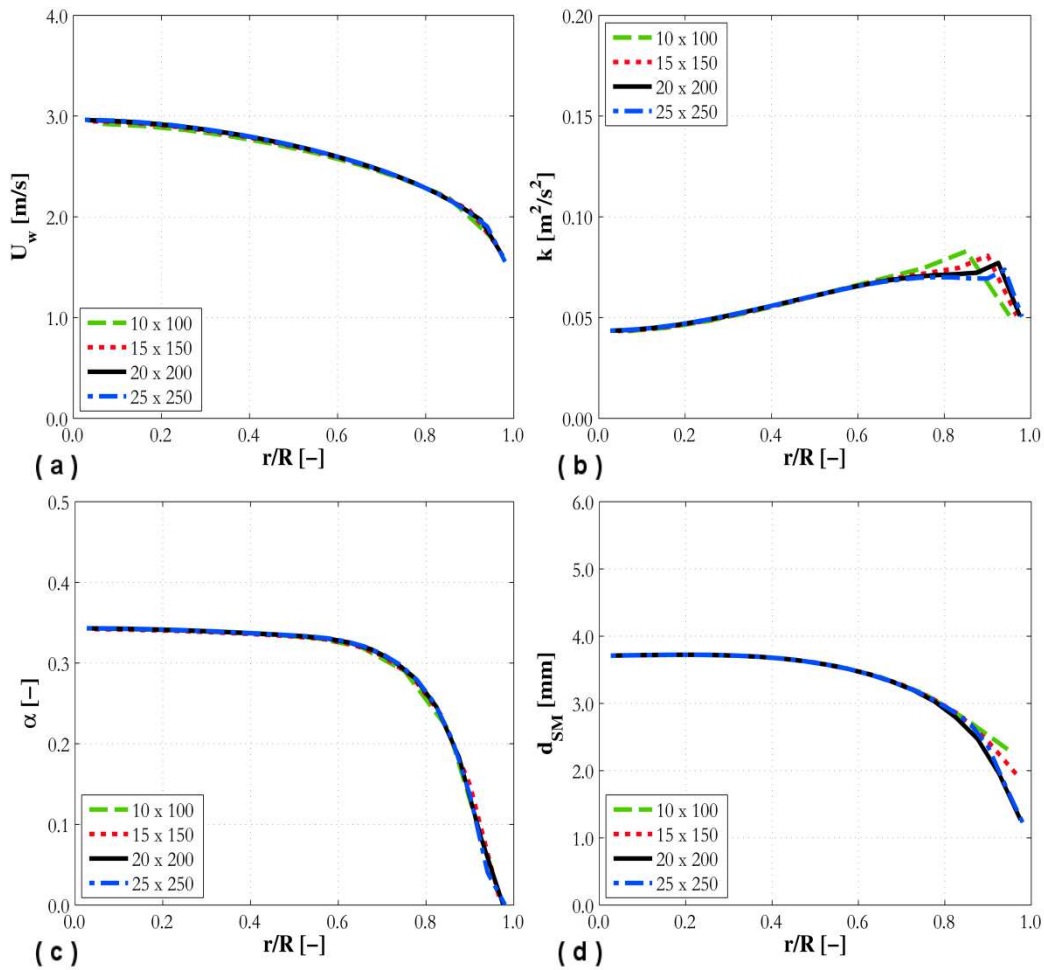
461

462 In the previous equation, d_c is the critical diameter at which bubble behaviour changes from a
463 spherical bubble to a cap bubble.

464

465 The overall model, implemented in the STAR-CCM+ CFD code (CD-adapco, 2014), was solved in
466 a two-dimensional axisymmetric geometry. At the inlet, fully-developed phase velocities and void
467 fraction boundary conditions were imposed, together with an imposed pressure at the outlet and the
468 no-slip condition at the wall. Experimental measurements of average bubble diameter at the first
469 measurement station were used for the bubble diameter inlet boundary condition. Therefore,
470 experimental measurements at the last station were compared against predictions at a distance from
471 the inlet equal to that between the first and the last measurement stations. Strict convergence of
472 residuals was ensured, together with a mass balance error lower than 0.01 % for both phases.
473 Experiment HI2 was selected for a mesh sensitivity study, the results of which are presented in
474 Figure 1 in terms of the radial profiles of water velocity, turbulence kinetic energy, void fraction
475 and SMD. The radial profiles are shown as a function of the normalized radial position r/R , which is
476 equal to 0 at the pipe centre and to 1 at the pipe wall. Four grids were tested with a progressively
477 increasing number of grid nodes (10×100 , 15×150 , 20×200 , and 25×250). The water velocity
478 and void fraction distributions are rather insensitive to the number of nodes, but some differences
479 between the various grids are apparent for the turbulence kinetic energy and the SMD. From the
480 results in Figure 1, the grid with 20×200 nodes was chosen for other simulations. All grids had a

481 first grid node higher than, but close, to $y^+ = 30$, which is the lower limit for the use of wall
 482 functions.



483
 484 Figure 1. Mesh sensitivity study in terms of radial and axial node numbers for experiment HI2.
 485 Water velocity (a), turbulence kinetic energy (b), void fraction (c) and SMD (d) radial profiles are
 486 presented.
 487

488
 489 **4. Results and discussion**

490
 491 This section describes and discusses the simulation results and comparisons against experimental
 492 data. First, the experiments of Liu (1993), Hibiki and Ishii (1999) and Hibiki et al. (2001) were
 493 simulated with the YM model (Yao and Morel, 2004) and the results are presented in Figure 2 and
 494 Figure 3. As can be seen, the YM model generally overestimates the SMD. In particular, marked
 495 overestimations were obtained at the lowest liquid velocities (Hi1, HI1 and L1), whereas, at higher
 496 velocities (Hi2, HI2 and L2), the overestimation is reduced and, for experiment HI2 (Figure 3a)

497 only, good agreement with data is found. The tendency of the YM model to over-predict the bubble
498 diameter has already been noted by Cheung et al. (2007) and Nguyen et al. (2013). To serve as a
499 benchmark, predictions from the LZ model (Lo and Zhang, 2009) are also included in Figure 2 and
500 Figure 3. Overall, the LZ model provides better accuracy when predicting the SMD. Nevertheless,
501 and similar to YM, a strong dependency on the liquid velocity is apparent. At low velocity, good
502 agreement, or limited overestimation of the SMD, was obtained (with respect to YM) but, at higher
503 velocities, LZ under predicts the experiments. In addition, as already reported in Lo and Zhang
504 (2009), the bubble diameter is generally under predicted in the near wall region, probably as a
505 consequence of the excessively strong bubble break-up rate there.

506

507 The availability of experimental data allowed a further optimization of the YM model to be made.
508 As the over prediction of the bubble diameter is possibly due to an excessive amount of bubble
509 coalescence in the flow, this was limited by modifying the value of We_{crit} in Eq. (36), where it
510 mainly impacts the coalescence probability. Therefore, a lower We_{crit} reduces the coalescence
511 probability or, from a different perspective, it reduces the interaction time available to the liquid
512 film trapped between the two colliding bubbles to drain out. Calibration of the model was limited to
513 the coalescence model (the model for break-up was not changed from that of Lo and Zhang (2009),
514 except for the value of We_{crit} , equal to 1.24 for YM). Even if the SMD is still overestimated at low
515 liquid velocity and underestimated at high liquid velocity, acceptable agreement was achieved in all
516 the tested conditions with $We_{crit} = 0.10$ (YM opt. lines in Figure 2 and Figure 3). Overall, the
517 improvement in the accuracy with respect to the original YM and LZ models is significant. In the
518 near wall region, where LZ significantly under predicts the experimental data, the value of the
519 bubble diameter is well predicted, with the exception of experiment HI1 (Figure 2g) in which the
520 flow rate is particularly low. In addition, for the LZ model, optimization on a case-by-case basis has
521 been found necessary to reach a comparable accuracy (Lo and Zhang, 2009), whereas, in this work,
522 the same value of We_{crit} was maintained for all flow conditions considered. In view of this finding,

523 additional research work is required to develop more general and accurate models of bubble break-
524 up and coalescence.

525

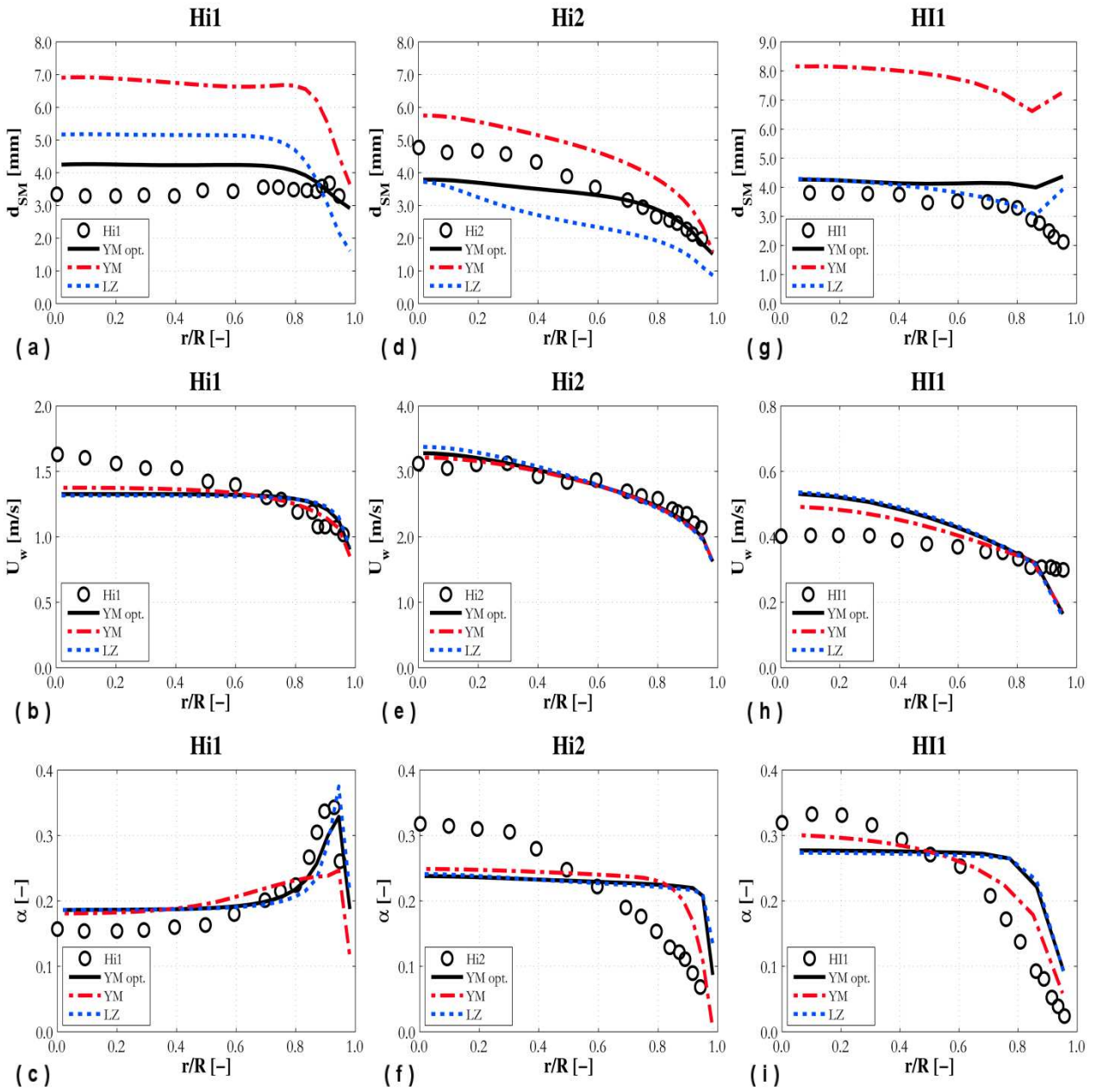
526 Figure 2 and Figure 3 also show radial profiles of the mean water velocity and void fraction (for L1
527 and L2, Figure 3e and Figure 3h, the air velocity is also provided). Overall, simulation results are in
528 good agreement with the experiments. The mean velocity is under predicted for L2 and, but only in
529 the pipe core region, for Hi1. With regards to the void fraction, the best agreement is found for the
530 wall-peaked void profiles (Figure 2c, Figure 3f and Figure 3i). In contrast, the core-peaked void
531 profiles were more difficult to predict. As it is possible to see from Figure 2 and Figure 3, a larger
532 bubble size spectrum characterizes the core-peaked void profiles (Hi2, HI1 and HI2) with respect to
533 the wall-peaked profiles, where the average bubble diameter radial distribution is generally flatter.
534 This complicates the simulation of the momentum transfer at the interphase, even with the use of a
535 population balance model. As shown in Figure 2f, Figure 2i and Figure 3c, a sharp increase in the
536 near wall region, followed by an almost flat profile, is usually predicted. The experiments, however,
537 show a more gentle but continuous increase of the void fraction towards the pipe centre. Predictions
538 are similar amongst the three different models considered. This suggests that it is the interphase
539 momentum forces (lift and wall forces in particular) that mostly determine the radial void fraction
540 and mean velocity profiles. In this regard, the use of constant lift force coefficients, not dependent
541 on the bubble diameter, may significantly inhibit changes in the lift force induced by changes in the
542 latter diameter.

543

544 The role of the critical Weber number in the YM model is the focus of the results given in Figure 4,
545 where the SMD profile is shown for three different values of We_{crit} . It has already been mentioned
546 how We_{crit} mainly affects the coalescence probability. Specifically, a lower We_{crit} reduces the
547 coalescence probability and, therefore, the average bubble diameter. This effect is equivalent to
548 reducing the interaction time available for the liquid film trapped between two colliding bubbles to

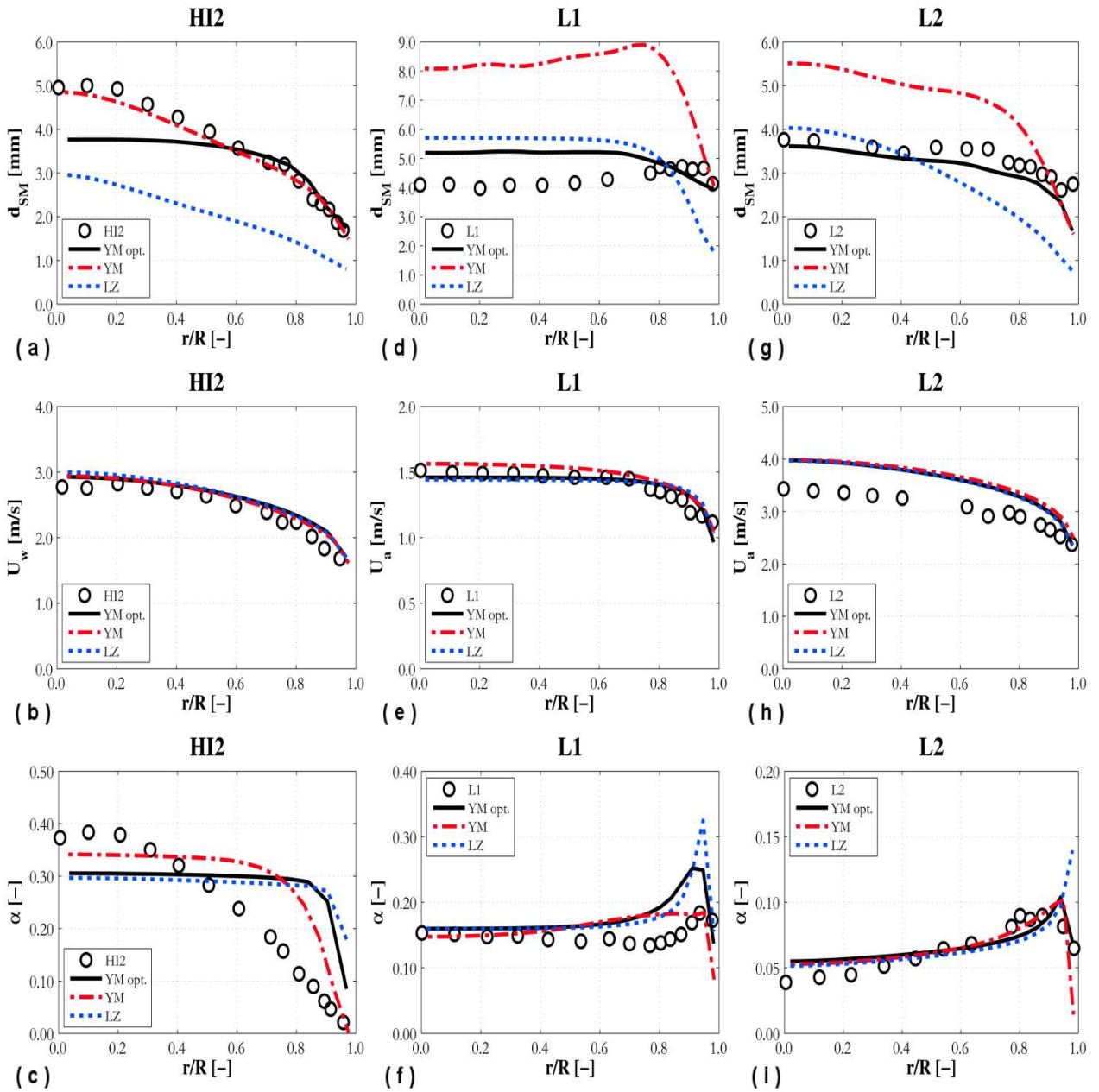
549 drain out, or, equivalently, to increasing the time required by this liquid film to drain out. Figure 4
550 includes two different experimental datasets. It is observed that the reduction in coalescence with
551 We_{crit} is higher at the low flow rate (Figure 4a), while the effect of a lower We_{crit} is reduced at the
552 higher flow rate (Figure 4b). At high flow rates, therefore, the interaction time is low given the high
553 level of turbulence, and hence the coalescence probability has a correspondingly low value. As a
554 consequence, the amount of decrease achievable by tuning We_{crit} is also low. At low flow rates, in
555 contrast, the coalescence probability is higher due to the longer interaction times that occur in a low
556 level turbulence field, and hence this probability can be significantly affected by a change in the
557 value of We_{crit} .

558
559



560
 561
 562
 563
 564
 565

Figure 2. SMD, mean water velocity and void fraction radial profiles compared against experiments Hi1 (a-c), Hi2 (d-f) and HI1 (g-i). Simulation results are shown for LZ (---), YM (---) in its standard form (Eq. 36) and after optimization (YM opt., —).



566
567
568
569
570
571

Figure 3. SMD, mean velocity and void fraction radial profiles compared against experiments HI2 (a-c), L1 (d-f) and L2 (g-i). Simulation results are shown for LZ (---), YM (---) in its standard form (Eq. 36) and after optimization (YM opt., —).

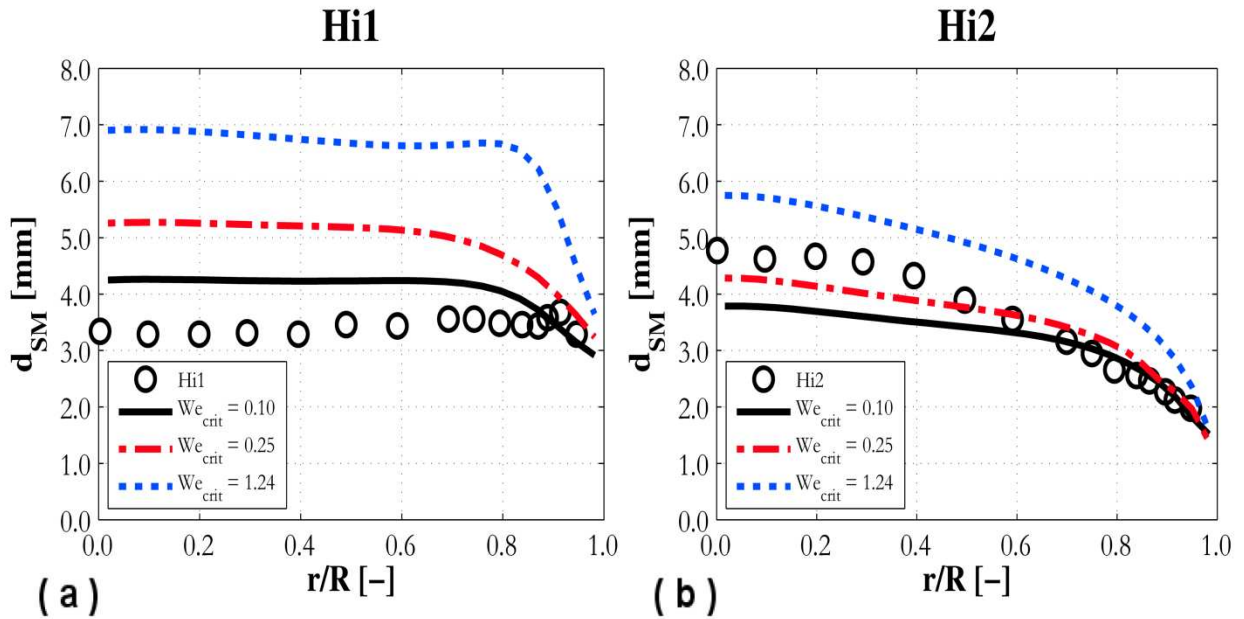


Figure 4. SMD radial profiles obtained with YM and $We_{crit} = 0.1$ (—), $We_{crit} = 0.25$ (---) and $We_{crit} = 1.24$ (···). Predictions are compared against experiments Hi1 (a) and Hi2 (b).

4.1. Effect of the break-up model

As mentioned, no changes were introduced in the break-up model, except for the value of the We_{crit} , which, for YM, was increased to 1.24 following the authors' proposal (Yao and Morel, 2004). Since no clear indications of the amount of bubble break-up occurring are available for the flows studied in this work, additional simulations neglecting break-up were made to evaluate the impact of the break-up model on the predictions. In Figure 5, four of the experiments were predicted with and without accounting for break-up. For the majority of the pipe cross-section, the effect of break-up on the bubble diameter distribution is seen to be negligible. In the near wall region, break-up is effective in reducing the SMD, but only at the highest liquid velocities (Figure 5b and Figure 5d). At low velocities, break-up is negligible even in the region close to the wall (Figure 5a and Figure 5c). Overall, and in view of the agreement obtained with these experiments, these results suggest that coalescence is the dominant mechanism in these flows.

Since only the net result of the combined action of both break-up and coalescence is available in terms of the experimental data, this being the SMD, additional sensitivity studies were made,

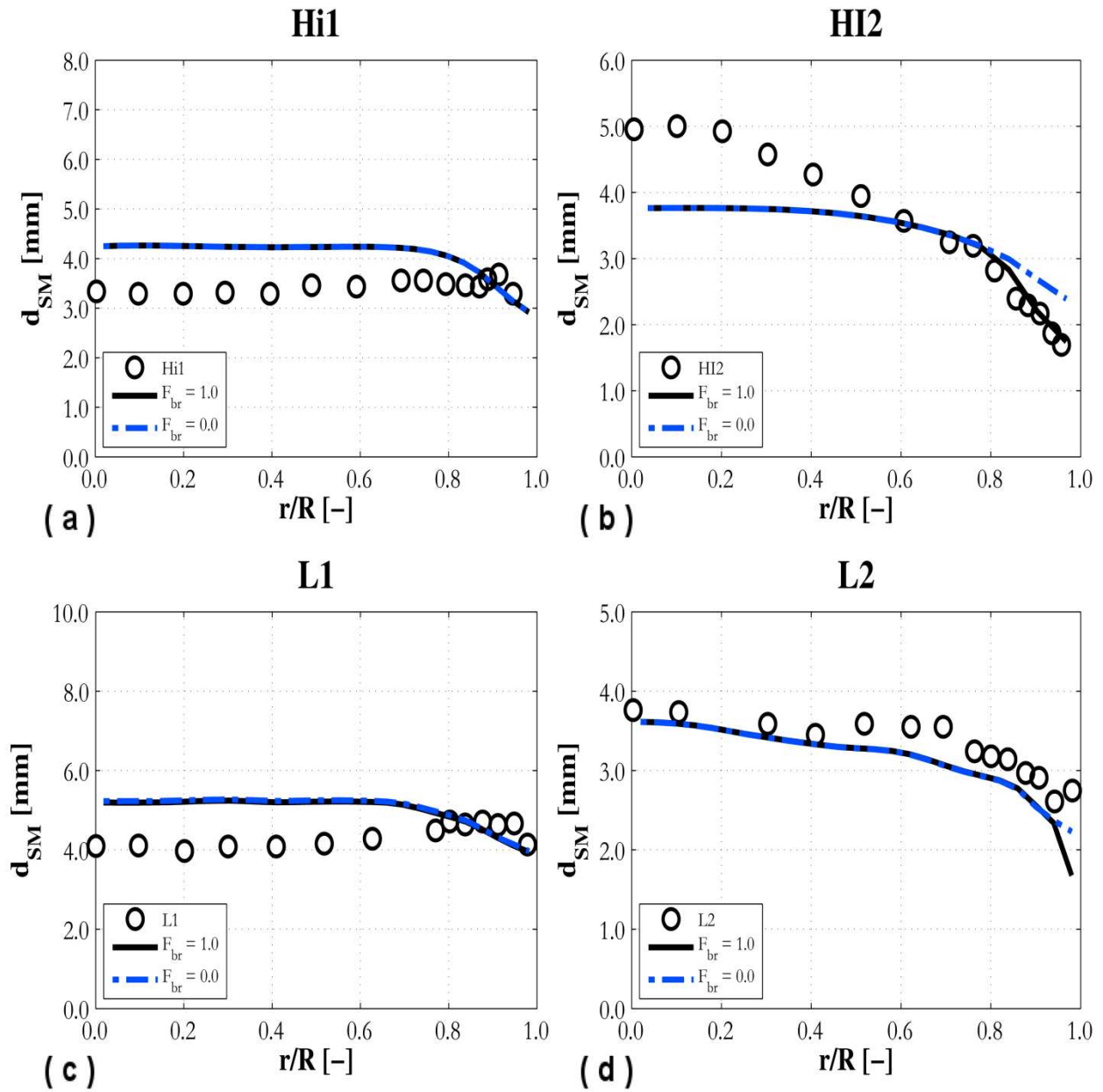
592 increasing the impact of both. The same We_{crit} value of 0.25 was adopted in both the break-up and
593 the coalescence models. The increase in the rate of coalescence with a higher critical Weber number
594 was already addressed in Figure 4. A lower We_{crit} in the break-up model increases the break-up rate
595 since a lower energy is required to break-up the bubble. The value of We_{crit} adopted is now close to
596 that used in the LZ model and, therefore, a comparable amount of break-up is to be expected. The
597 results are presented in Figure 6. Even if some improvement is obtained for a number of flows
598 (Figure 6a, Figure 6c and Figure 6e), excessive break-up causes an under prediction of bubble
599 diameter at high liquid velocities (Figure 6b, Figure 6d and Figure 6f). In addition, and except for
600 experiment HI1 (Figure 6c), the bubble diameter is always underestimated in the near wall region,
601 where, in view of the higher levels of turbulence, break-up is expected to be more significant.
602 Again, these results are similar to those obtained with the LZ model (Figure 2 and Figure 3), for
603 which an excessive amount of break-up, in particular in the near wall region, has already been
604 reported (Lo and Zhang, 2009). This further supports the case for these flows being coalescence
605 dominated.

606 Overall, and despite the previous results, it remains difficult to precisely evaluate the accuracy of
607 the model with regard to the competitive action of coalescence and break-up, and the mechanisms
608 involved. As mentioned, only the net result is available through data on the bubble diameter.
609 Therefore, additional knowledge is required on the physics of these flows, and on the interaction
610 between bubbles and with the continuous phase in particular. The lack of information on these
611 processes is a significant constraint on the further development of these models that needs to be
612 overcome if more accurate modelling is to be achieved. As an example, the recent tendency has
613 been to include all possible mechanisms of bubble break-up and coalescence (e.g. turbulent
614 collision, wake entrainment, shearing-off) (Liao et al., 2015; Smith et al., 2012; Sun et al., 2004).
615 Even if this may benefit the generality of the developed models, the relative influence of each
616 mechanism has been generally optimized with additional constants tuned against average bubble
617 diameter measurements, which, at the present time, is the only real option available to modellers.

618 Without a clear knowledge of the effective impact of each mechanism as a function of the flow
619 conditions, however, accurate prediction of the average bubble diameter does not guarantee the
620 accuracy of each individual model, and possibly increases the uncertainty in the results and limits
621 the applicability of the model itself. In view of this, advances must rely on the availability of more
622 detailed experimental measurements or, perhaps, accurate direct numerical simulations of bubble
623 behaviour.

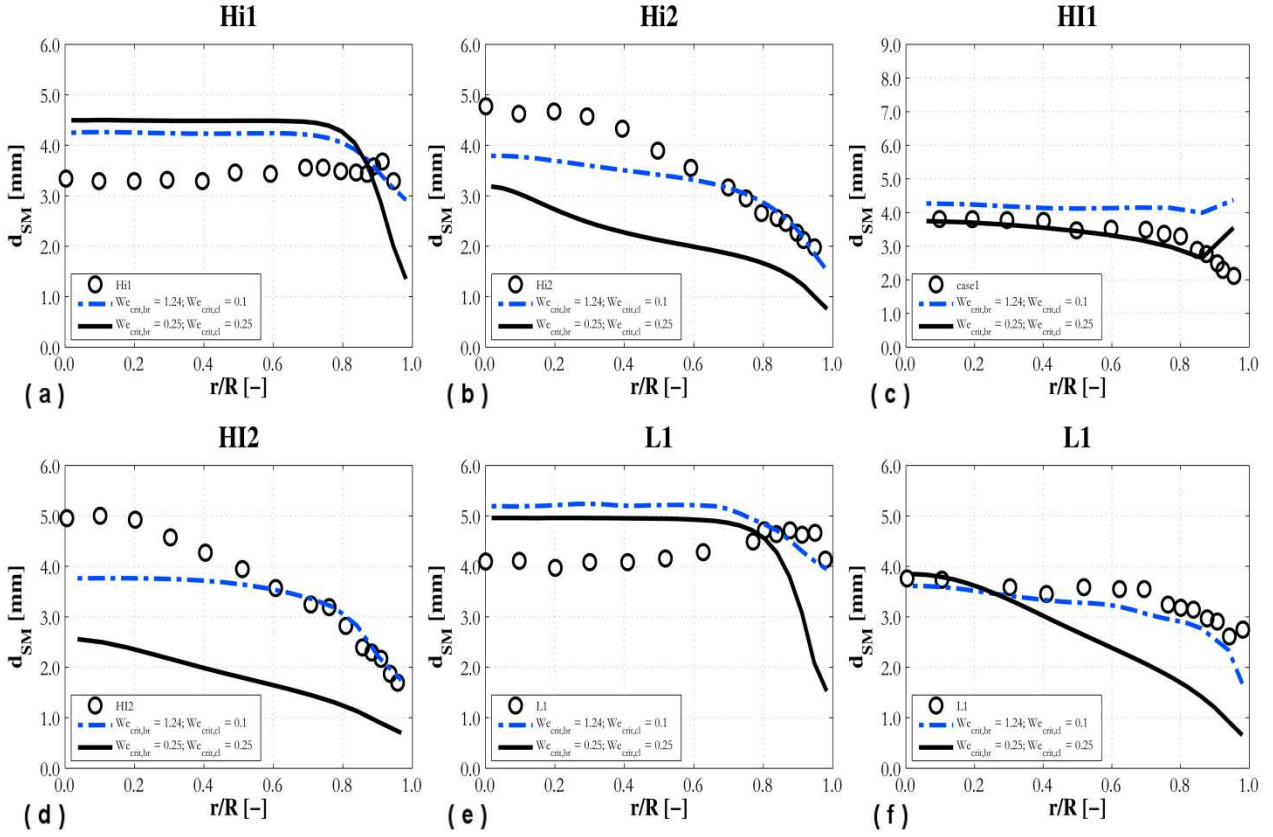
624

625



626
627
628
629

Figure 5. SMD radial profiles with (—) and without (---) considering the effect of bubble break-up in the flow. Predictions are compared against experiments Hi1 (a), Hi2 (b), L1 (c) and L2 (d).



630
 631 Figure 6. SMD radial profiles at different rates of coalescence and break-up of bubbles in the flow
 632 ($We_{crit,br} = 1.24$ and $We_{crit,cl} = 0.1$ (—); $We_{crit,br} = 0.25$ and $We_{crit,cl} = 0.25$ (---)). Predictions are
 633 compared against the experiments in Table 1.
 634

635 4.2. Continuous phase turbulence sensitivity

636
 637 Turbulence parameters affect in different ways the models for coalescence and break-up, and, as the
 638 latter models are based on the collision of bubbles due to turbulence, they are expected to have a
 639 significant impact on results. The sensitivity to the turbulence model predictions has already been
 640 investigated in some literature studies (Nguyen et al., 2013; Yao and Morel, 2004), but, in many
 641 more, the assessment and optimization of the coalescence and break-up models was carried out
 642 without considering the accuracy of the turbulence predictions. The aim of this section, therefore, is
 643 to address the dependency of results on the continuous phase turbulence.
 644

645 In bubbly flows, the contribution of the bubbles to the continuous phase turbulence is accounted for,
 646 in the $k-\varepsilon$ turbulence model, by source terms in the equations of that model (Eq. (11) and Eq. (12),
 647 Section 3.1).

648

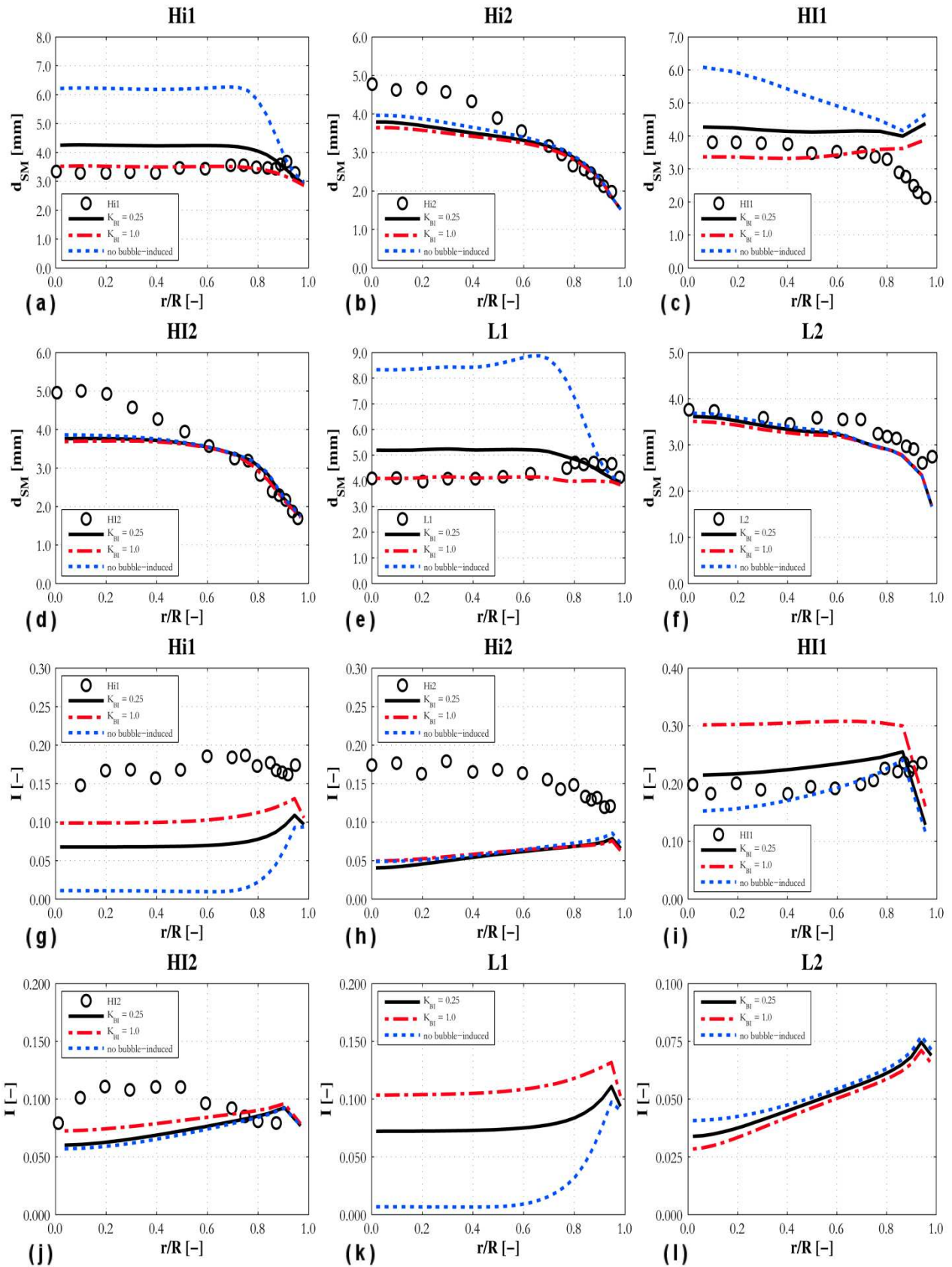
649 Figure 7 shows radial profiles of the predicted SMD as a function of the amount of bubble-induced
650 turbulence, together with the continuous phase streamwise turbulence intensities I . Turbulence
651 measurements are available only from Hibiki and Ishii (1999) and Hibiki et al. (2001), where
652 turbulence intensity was calculated by dividing the streamwise r.m.s of the velocity fluctuations by
653 the maximum liquid velocity. Three different cases are considered: no bubble-induced turbulence,
654 and Eq. (14) with $K_{BI} = 0.25$ and $K_{BI} = 1.0$. At low flow rates (HI1, Figure 7i), or for wall-peaked
655 void profiles (Hi1, Figure 7g, and L1, Figure 7k), where the presence of the bubbles induces a flat
656 mean velocity profile and a strong reduction of the shear-induced turbulence production in the pipe
657 centre, the contribution of the bubble-induced turbulence is significant. For the high flow rate wall-
658 peaked case (L2, Figure 7l), where the turbulence level is already high and the void fraction in the
659 pipe centre is low, and the core-peaked void profiles (Hi2, Figure 7h, and HI2, Figure 7j), where the
660 shear-induced production remains significant, the impact of the bubble-induced contribution is less.
661 In the first case scenario, significant differences in the turbulence level cause bubble diameter
662 profiles to be very different from one another (Figure 7a, Figure 7c and Figure 7e). This means that
663 these results are dependent on the continuous phase turbulence and, for some flows, on the bubble-
664 induced turbulence model as well. Therefore, for a proper model validation, both the average
665 bubble diameter and the continuous phase turbulence predictions need to be compared against
666 experiments. Conversely, the results may be dependent not only on the flows used for validation,
667 but also on the specific bubble-induced turbulence model. Unfortunately, turbulence measurements
668 are not available for all the experiments considered. Moreover, for the data of Hibiki et al. (2001),
669 turbulence levels were always under predicted, even when considering all the drag force to be
670 converted to turbulence kinetic energy. It must be pointed out that the turbulence intensities in these
671 data appear significantly higher than for other experiments in the literature having comparable
672 geometry and flow conditions (Liu, 1998; Serizawa et al., 1975; Wang et al., 1987). For HI1 and
673 HI2, instead, satisfactory predictions were obtained. In view of the limited number of simultaneous

674 measurements of both the bubble diameter distribution and the flow turbulence, some additional
675 comparisons are shown in Figure 8, taking advantage of a previous validation of the bubble-induced
676 turbulence model (Eq. (14) and Eq. (15)), which showed satisfactory accuracy over a wide range of
677 conditions (Colombo and Fairweather, 2015). In Figure 8, radial profiles of the r.m.s. of streamwise
678 velocity fluctuations are compared against different bubbly flow data in vertical pipes. For these
679 validations, the bubble diameter was fixed and assumed equal to experimental observations, even if
680 only rough averaged values were available for the majority of the experiments. Even if some
681 discrepancies are still apparent, the overall agreement can be considered satisfactory. This
682 additional validation, although useful, did not allow a comparison of bubble diameter and
683 turbulence for the same experiment and, therefore, concerns related to data availability still remain.
684 Recently, the development of advanced experimental techniques has allowed detailed
685 measurements of the average bubble diameter and the bubble diameter distribution (Lucas et al.,
686 2005, 2010; Prasser et al., 2007). However, in view of the previous results and to better support the
687 modelling effort, experimental measurements need to allow not only the validation of the bubble
688 diameter distribution, but also of the continuous phase turbulence level.

689

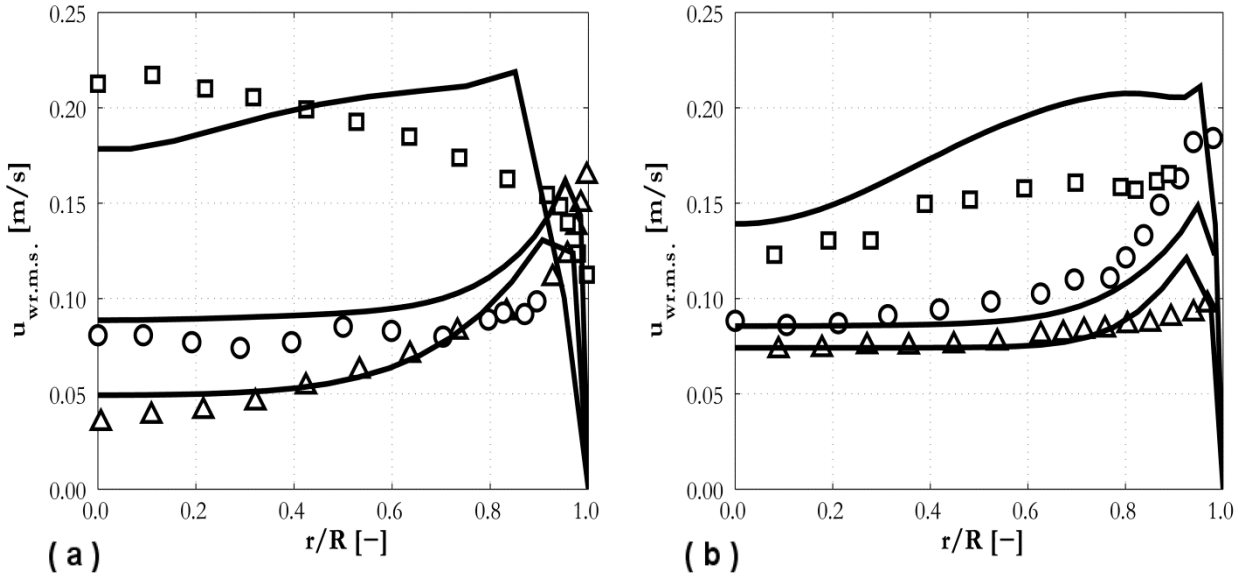
690 In Figure 7, YM predicts a higher SMD, therefore a higher coalescence ratio, with a decrease in the
691 continuous phase turbulence. Collision rate increases with turbulence, while coalescence probability
692 reduces, with the latter being the dominant effect. This qualitatively behaviour needs further
693 examination. In Figure 9, the same sensitivity study is made for the LZ model, for experiments Hi1,
694 Hi2 and L1. The turbulence intensity behaviour remains the same, but the bubble diameter
695 predictions are changed. At low liquid velocity (Hi1 and L1) and without the bubble-induced
696 turbulence model, bubble diameter is high at the wall, where the turbulence remains high, whereas
697 it is low in the centre of the pipe due to the reduced turbulence in this region. When the turbulence
698 level is increased, the coalescence is also increased, and, consequently, the SMD. With a further
699 increase of the turbulence, the bubble diameter is reduced by a decrease of the coalescence or, more

700 likely, by an increase of bubble break-up, which is higher for this model (Section 4.2). At high
701 velocity (Hi_2), the break-up is already high even without including bubble-induced turbulence.
702 Therefore, with an increase of the turbulence level, the break-up is further increased and a decrease
703 of the SMD is observed. For YM, even if a reduction in the coalescence following an increase of the
704 turbulence, at already high turbulence levels, cannot be excluded, in the limit of zero turbulence, an
705 increase of the coalescence is expected following an increase in the turbulence. Therefore, despite
706 the good accuracy shown, the qualitative behaviour of YM with the turbulence level, which is
707 different from that of LZ, suggests the need for additional future verification of these models.

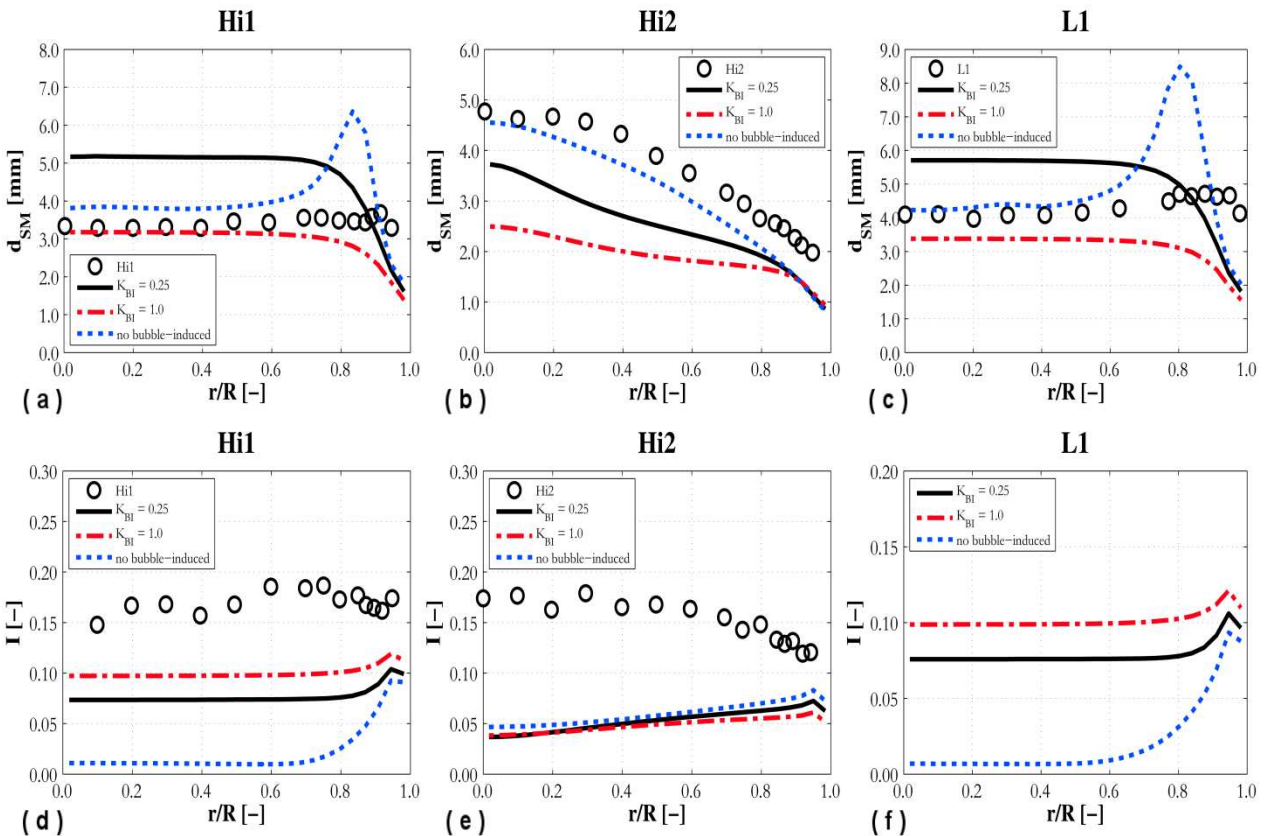


708
709
710
711
712

Figure 7. SMD (a-f) and turbulence intensity (g-l) radial profiles without bubble-induced turbulence (---), and with bubble-induced turbulence, and for $K_{BI} = 0.25$ (—) and $K_{BI} = 1.0$ (---). Predictions, obtained with YM and $We_{crit} = 0.1$, are compared against experiments in Table 1.



713
 714 Figure 8. Radial profiles of r.m.s. of streamwise velocity fluctuations compared against experiments
 715 in bubbly pipe flows (Colombo and Fairweather, 2015). (a) Liu and Bankoff (1993), $j_w = 1.087$ m/s,
 716 $j_a = 0.112$ m/s (Δ); Serizawa et al. (1975), $j_w = 1.03$ m/s, $j_a = 0.291$ m/s (\circ); Liu and Bankoff (1993),
 717 $j_w = 0.376$ m/s, $j_a = 0.347$ m/s (\square). (b) Wang et al. (1987), $j_w = 0.71$ m/s, $j_a = 0.1$ m/s (Δ); Liu
 718 (1998), $j_w = 1.0$ m/s, $j_a = 0.22$ m/s (\circ); Serizawa et al. (1975), $j_w = 1.03$ m/s, $j_a = 0.436$ m/s (\square).
 719



720
 721 Figure 9. SMD (a-c) and turbulence intensity (d-f) radial profiles without bubble-induced
 722 turbulence (---), and with bubble induced turbulence, and for $K_{BI} = 0.25$ (—) and $K_{BI} = 1.0$ (---).
 723 Predictions, obtained with LZ, are compared against experiments Hi1 (a,d), Hi2 (b,e) and L1 (c,f).
 724

725 4.3. Reynolds stress turbulence model

726
727 Using the YM model, the same tests were repeated with a Reynolds stress turbulence model and the
728 results are presented in Figure 10 and Figure 11. A comparable level of agreement with data is
729 found using both turbulence models for the SMD profiles (Figure 10 a-c and Figure 11 a-c), and
730 similar velocity profiles were obtained (Figure 10 d-f and Figure 11 d-f). Similar void fraction
731 profiles were also obtained for the wall-peaked cases (Figure 10g, Figure 11h and Figure 11i),
732 although for the core-peaked profiles, the behaviour of the void fraction is reproduced better by the
733 RSM (Figure 10h, Figure 10i and Figure 11g). More specifically, in such cases the void fraction
734 gently increases from the wall towards the pipe centre. However, for the $k-\varepsilon$ model, the increase is
735 sharper near the wall, and the profile is then flatter towards the pipe centre. In a turbulent bubbly
736 flow, the turbulence may interact with the interphase forces, inducing a radial pressure gradient in
737 the flow that impacts upon the distribution of the dispersed phase (Ullrich et al., 2014). Generally,
738 since the turbulence is higher near the wall, the pressure accordingly increases towards the pipe
739 centre. It is this pressure gradient that is likely responsible for the over predicted void fraction peak
740 for experiment L2 (Figure 11i).

741
742 In bubbly pipe flows, the turbulence is anisotropic, and this anisotropy can be reproduced using a
743 Reynolds stress model (Colombo and Fairweather, 2015). Therefore, different results should be
744 expected when using a $k-\varepsilon$ model, because of the different turbulent stresses, or if the turbulence
745 kinetic energy is added to the pressure. It must be noted, however, that differences between the two
746 turbulence modelling approaches might be obscured by the influence of the interfacial momentum
747 forces, which have been the object of a significant amount of optimization and refinement in the
748 past. It is the opinion of the authors, however, that even when a similar accuracy is obtained (wall-
749 peaked profiles), the use of a Reynolds stress formulation provides more insight into the distinctive
750 features of the flow and should assist the development of models of more general applicability. In

751 this regard, Ullrich et al. (2014) predicted some wall-peaked void fraction profiles with an RSM,
752 whilst neglecting lift and wall reflection forces.

753

754 Differences between the turbulence model predictions are also apparent in the turbulence intensity
755 profiles (Figure 10 j-1 and Figure 11 j-1). These, even if small for the majority of cases, induce
756 differences in the coalescence rates which, as discussed in the previous section, are strongly
757 dependent on the turbulence in the continuous phase. The different coalescence rates, together with
758 differences in the void fraction profiles, can be considered the reason for the slight disparity in the
759 bubble diameter and the mean velocity profiles between the $k-\varepsilon$ model and the RSM.

760

761

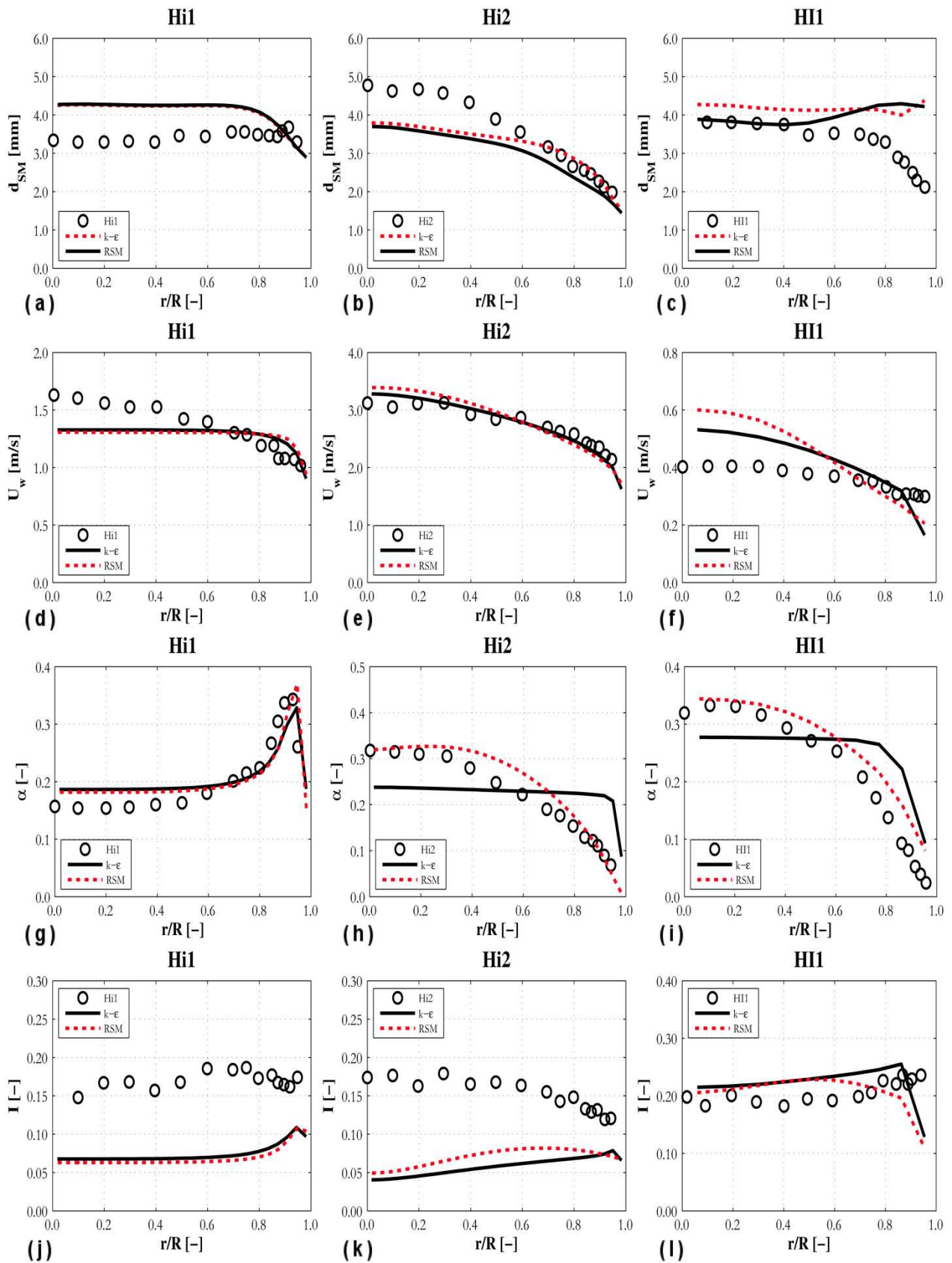


Figure 10. SMD (a-c), mean velocity (d-f), void fraction (g-i) and turbulence intensity (j-l) radial profiles compared against experiments Hi1, Hi2 and HI1. Predictions were obtained with a $k-\epsilon$ (—) and a Reynolds stress (---) turbulence formulation.

762
763
764
765

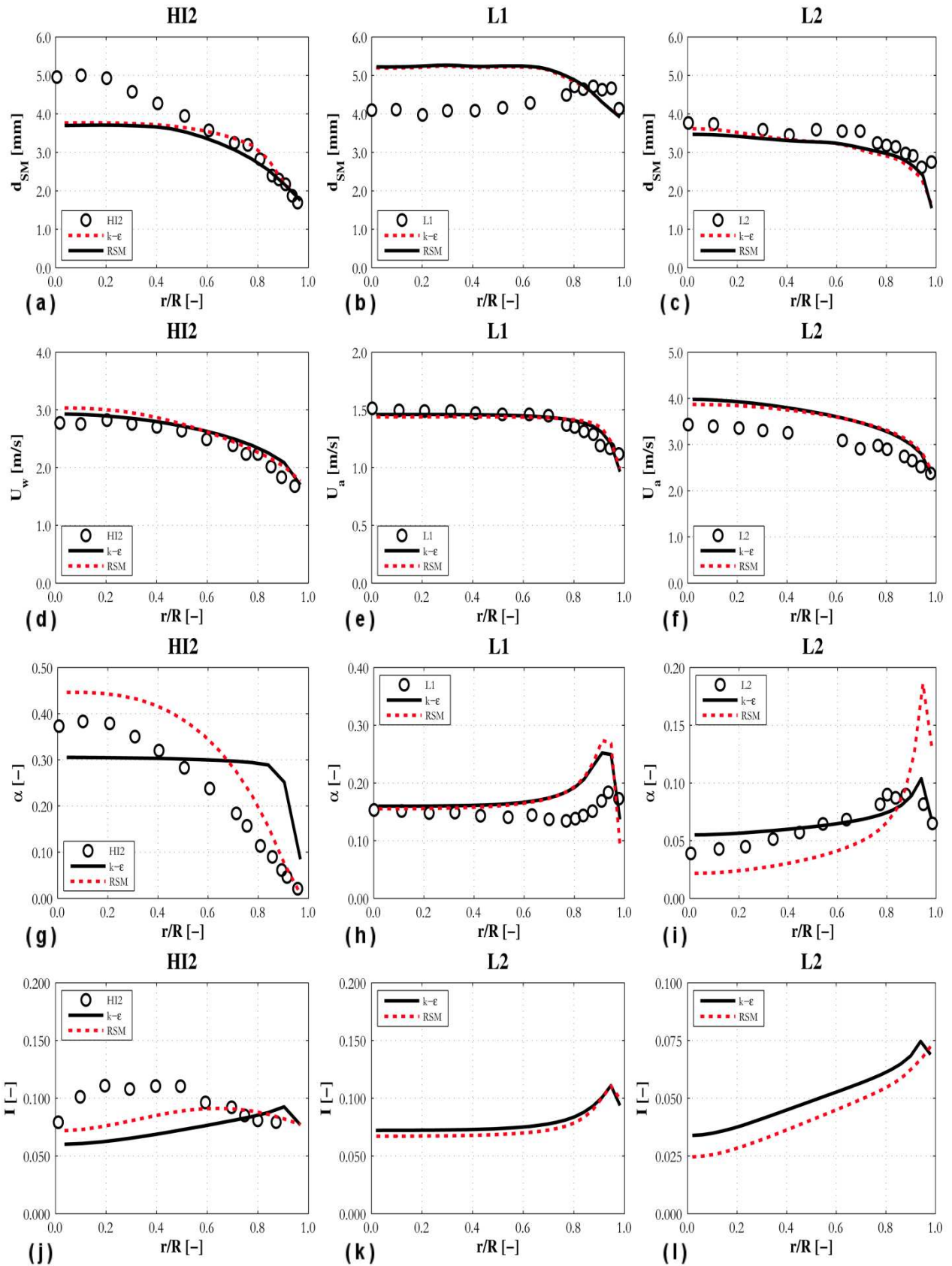


Figure 11. SMD (a-c), mean velocity (d-f), void fraction (g-i) and turbulence intensity (j-l) radial profiles compared against experiments HI2, L1 and L2. Predictions were obtained with a $k-\epsilon$ (—) and a Reynolds stress (---) turbulence formulation.

766
767
768
769
770

771 4.4. Two-group model

772
773 It was mentioned in the introduction how bubbly flows are generally characterized by polydispersity
774 and by an extended range of bubble sizes. The comparisons in the previous sections demonstrated
775 the different behaviour of spherical and larger cap bubbles, showing wall-peaked or core-peaked
776 void fraction profiles induced by the value of the average bubble diameter. When both types of
777 bubble are present in a comparable amount, the void fraction profile may exhibit both wall- and
778 core-peaked features, as is the case for the experiment L1, depicted in Figure 12 (Lucas et al.,
779 2005). These experiments are particularly difficult to predict because the distinctive features of both
780 bubble types must be reproduced. Therefore, an advanced model with two different bubble classes
781 was specifically implemented to predict these kinds of flows. In view of the results from the
782 previous sections, and the in general negligible impact of break-up, only the additional sources due
783 to the coalescence of two spherical bubbles into a cap bubble were considered. For this case, the
784 value of the critical diameter d_c was assumed equal to 5 mm. Comparison against experimental data
785 is provided in Figure 12, based on the RSM predictions. As shown in the figure, the void fraction
786 radial profile and the behaviour of both the spherical and the cap bubbles are well predicted. Near
787 the wall, the void fraction profile increases rapidly because of the presence there of the majority of
788 the spherical bubbles. After a region where it remains almost flat, the void fraction increases again
789 towards the pipe centre where the cap bubbles accumulate, pushed there by the negative lift force.
790 In a similar manner, close to the wall, the SMD is close to the SMD of the spherical bubbles,
791 whereas it tends to the SMD of the cap bubbles towards the pipe centre.

792
793 The bubble size distribution, which is tracked by the S_y model, is shown at three different axial
794 locations in Figure 13. The plots display h_{dB} , which is, following the work of Lucas et al. (2005),
795 the contribution of each bubble size to the total void fraction:

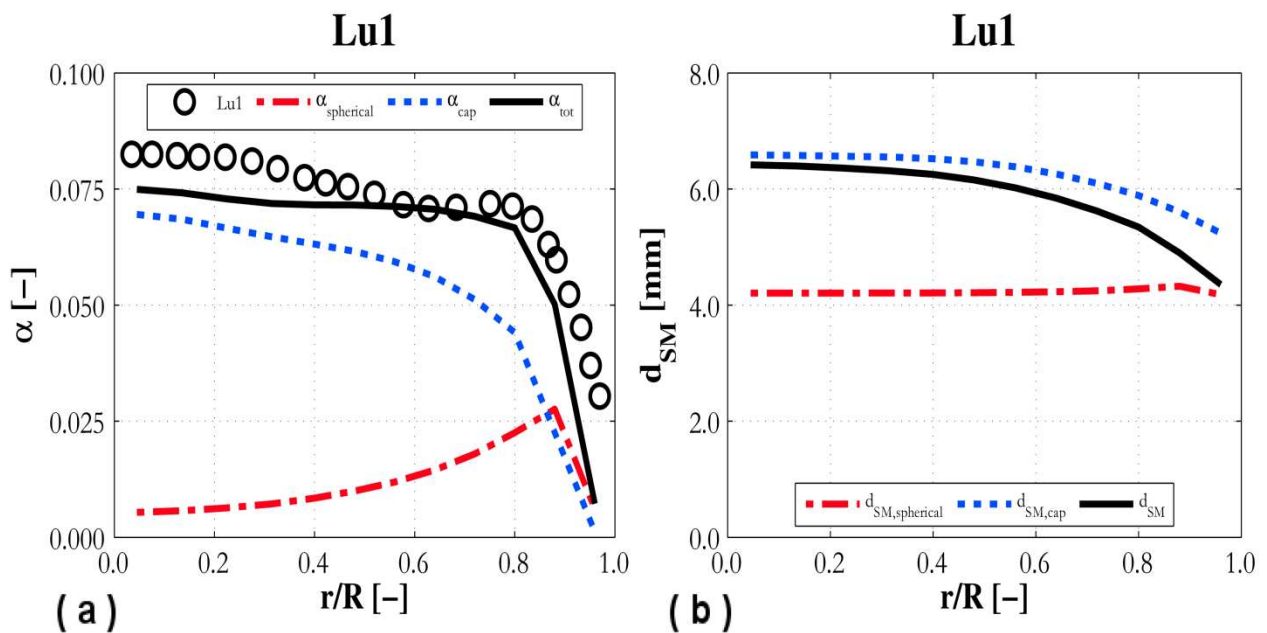
796

$$h_{d_B} = \frac{d(\alpha)}{d(d_B)} \quad (44)$$

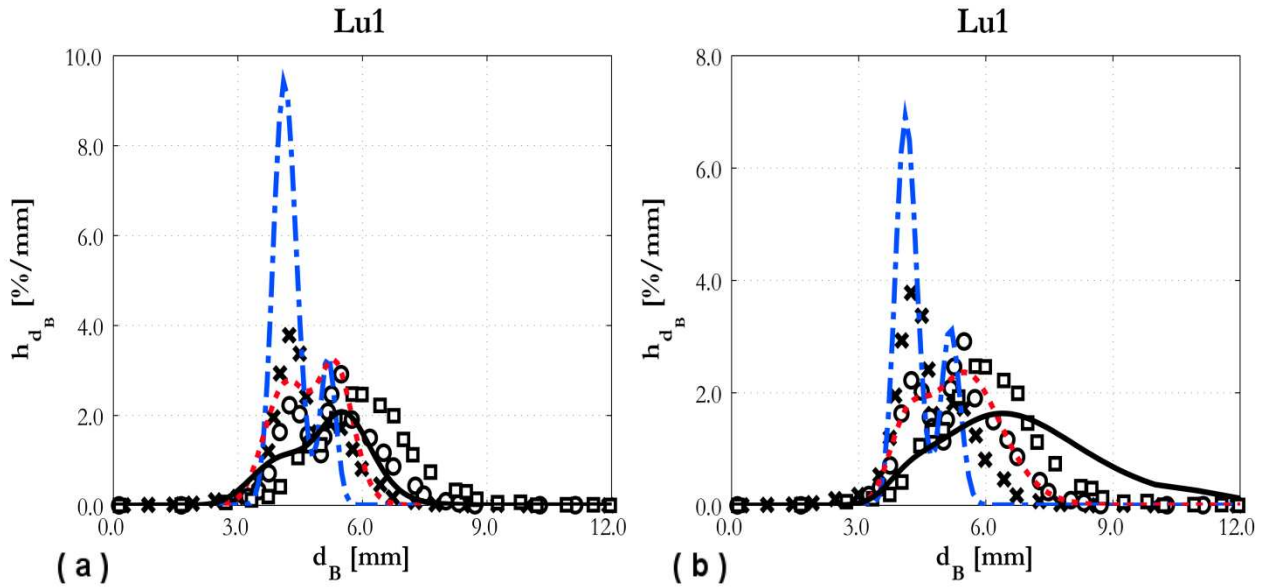
797

798 In this way, the contribution of larger bubbles, which are few in number but carry a significant
799 amount of the total air volume, is properly accounted for (Lucas et al., 2005). Experimental data
800 were obtained by averaging over the whole pipe cross-section. For the predictions, the bubble
801 distribution was extracted from the simulation at each node and is shown in Figure 13 for the near-
802 wall region (Figure 13a) and for the pipe centre (Figure 13b). At the first axial location ($L/D = 8.4$),
803 two distinct peaks are shown in both the experimental and the numerical results. Starting from the
804 inlet, the predominance of coalescence events leads to the formation of larger bubbles, as is
805 demonstrated by the second peak in the profile at around 6 mm. Obviously, being still close to the
806 inlet, large bubbles represent only a small fraction of the total void fraction. At this location, the
807 total void fraction is overestimated, as can be seen from the higher peak values predicted. This is
808 due to the fact that it was not possible to match the inlet conditions of the experiment exactly due to
809 lack of data, in particular for the velocity of the phases. Therefore, some distance from the inlet is
810 required for the flow to establish. Predicted values of the void fraction at the two other locations are
811 indeed significantly closer to the experimental values. At the second axial location ($L/D = 29.9$), the
812 bubble population evolves and, since coalescence remains predominant, the number of larger
813 bubbles increases. Two distinctive peaks are still present, but the larger diameter peak is now the
814 greatest. This shift of the bubble diameter spectrum to larger values is well reproduced by the
815 simulation, with the main difference with experiment being a larger number of bubbles in the region
816 between the two peaks. At the final location ($L/D = 59.2$), the larger bubbles are in the majority,
817 with the first peak at around 4 mm now being very small. The same evolution is found in the
818 simulation, with a more diffuse distribution and an extended spectrum of diameters. It should be
819 noted that the variance of the distribution is lower and the first peak still present near the wall where
820 the majority of the spherical bubbles are present. In contrast, near the pipe centre, where the

821 majority of the larger bubbles accumulate, the averaged experimental spectrum is overestimated and
 822 the bubble population extends to even higher values of the bubble diameter. The experimental
 823 profile, therefore, can be qualitatively considered an average of these two behaviours. In view of
 824 these results, the evolution of the bubble diameter distribution is predicted with a satisfactory
 825 accuracy, even with the rather simple model adopted which could be subject to numerous further
 826 improvements. Therefore, the challenge of predicting the whole bubble size spectrum from small
 827 spherical to large cap bubbles seems to be manageable with the use of only two bubble groups.
 828



829
 830 Figure 12. Void fraction (a) and SMD (b) radial profiles considering two bubble classes. Along with
 831 total values (—), which are compared against Lu1 experiment, predictions for spherical (---) and
 832 cap bubbles (---) are also shown.
 833



834
 835 Figure 13. Bubble diameter distribution extracted from the simulations (lines) compared against the
 836 experiments (markers) at three axial locations: $L/D = 8.4$ (x, ---); $L/D = 29.9$ (o, --); $L/D = 59.2$ (□,
 837 —). Simulation results are displayed in two different locations: (a) pipe wall; (b) pipe centre.
 838

839

840 5. Conclusions

841

842 In this work, the S_γ model (Lo and Zhang, 2009), based on the moments of the bubble size
 843 distribution, was coupled with an Eulerian-Eulerian two-fluid model with the STAR-CCM+ code,
 844 and tested against the data from seven upward bubbly flow experiments in pipes. Through the S_γ
 845 model, the evolution of the bubble size distribution was followed through the flows, so that the
 846 average SMD and the interfacial area concentration, which are crucial for the prediction of the
 847 phase interactions, could be tracked. Being based on the method of moments, the S_γ model also has
 848 the advantage that the required computational resources are limited. The addition of a different
 849 coalescence model (Yao and Morel, 2004), based on the collision of bubbles in turbulence and on
 850 the film drainage model, and further optimized against the experiments, allowed reproduction of the
 851 experimental radial profiles of the SMD. More specifically, a constant critical Weber number value
 852 of 0.10 in the coalescence model was sufficient to obtain a satisfactory predictive accuracy.

853

854 A sensitivity study suggested a negligible effect of the bubble break-up model and the best results
 855 were achieved by considering these flows to be dominated by bubble coalescence. However, the

856 lack of availability of experimental data, limited to the average bubble diameter alone, constrains
857 research work in the field. In particular, it is extremely difficult to evaluate the competitive
858 contributions of break-up and coalescence, and to extend the modelling to cover all possible
859 mechanisms involved. Therefore, additional knowledge is required, by means of experiments or
860 direct numerical simulations. Continuous phase turbulence was noted to significantly influence the
861 predictions of the model. In this regard, validation of turbulence models needs to be carried out in
862 conjunction with that for the bubble diameter evolution, and requires the availability of additional
863 complete datasets. In addition, different coalescence models were found to display different
864 qualitative behaviour following changes in the flow field turbulence level, and this requires further
865 investigation.

866

867 Lastly, an advanced version of the overall model described was tested. This included a Reynolds
868 stress turbulence formulation and two groups of bubbles, accounting for spherical bubbles
869 accumulating close to the wall and cap bubbles migrating towards the pipe centre. The RSM, in
870 addition to performing better in flows where known shortcomings of two-equation turbulence
871 models are present, provides better accuracy in predicting core-peaked void fraction profiles and
872 properly accounts for the interaction between the turbulence and the interphase forces. Comparison
873 with a complex void fraction profile suggested that extension of the model to only two bubble
874 groups is sufficient to describe the whole bubble spectrum, and the bubbly flow regime up to the
875 transition to slug flow, even though additional comparisons with data are necessary.

876

877 **Acknowledgements**

878

879 The authors gratefully acknowledge the financial support of the EPSRC under grant EP/K007777/1,
880 Thermal Hydraulics for Boiling and Passive Systems, part of the UK-India Civil Nuclear
881 Collaboration. The authors are also grateful to Dr. Andrew Splawski and Dr. Simon Lo from CD-
882 adapco for the valuable technical and scientific support.

883

884 **References**

- 885 Antal, S.P., Lahey Jr, R.T., Flaherty, J.E., 1991. Analysis of phase distribution in fully developed
886 laminar bubbly two-phase flow. *Int. J. Multiphas. Flow* 17, 635-652.
- 887 Auton, T.R., 1987. The lift force on a spherical body in a rotational flow. *J. Fluid Mech.* 183, 199-
888 218.
- 889 Behzadi, A., Issa, R.I., Rusche, H., 2004. Modelling of dispersed bubble and droplet flow at high
890 phase fractions. *Chem. Eng. Sci.* 59, 759-770.
- 891 Buffo, A., Vanni, M., Marchisio, D.L., Fox, R.O., 2013. Multivariate Quadrature-Based Moments
892 Methods for turbulent polydisperse gas-liquid systems. *Int. J. Multiphas. Flow* 50, 41-57.
- 893 Burns, A.D., Frank, T., Hamill, I., Shi, J.M., 2004. The Favre averaged drag model for turbulent
894 dispersion in Eulerian multi-phase flows. 5th International Conference on Multiphase Flow,
895 Yokohama, Japan, May 30 – June 4, paper 392.
- 896 CD-adapco, 2014. STAR-CCM+® Version 9.06 User Guide.
- 897 Chester, A.K., 1988. Local coalescence rates in emulsions: a model for collision and film thinning
898 process when drop inertia dominates. BRITE Report I-31.
- 899 Chester, A.K., 1991. The modeling of coalescence processes in fluid-liquid dispersions: A review of
900 current understanding. *Chem. Eng. Res. Des.: T I Chem. Eng.-Lond.* 69(A), 259-270.
- 901 Cheung, S.C.P., Deju, L., Yeoh, G.H., Tu, J.Y., 2013. Modelling of bubble-size distribution in
902 isothermal gas-liquid flows: numerical assessment of population balance approaches. *Nucl. Eng.*
903 *Des.* 265, 120-136.
- 904 Cheung, S.C.P., Yeoh, G.H., Tu, J.Y., 2009. A review of population balance modelling for
905 isothermal bubbly flows. *J. Comput. Multiphas. Flow* 1, 161-199.
- 906 Cheung, S.C.P., Yeoh, G.H., Tu, J.Y., 2007. On the modelling of population balance in isothermal
907 vertical bubbly flows-Average bubble number density approach. *Chem. Eng. Process.* 46, 742-756.
- 908 Colombo, M., Fairweather, M., 2015. Multiphase turbulence in bubbly flows: RANS simulations.
909 *Int. J. Multiphas. Flow* 77, 222-243.

910 Colombo, M., Fairweather, M., Lo, S., Splawski, A., 2015. Multiphase RANS simulation of
911 turbulent bubbly flows. 16th International Topical Meeting on Nuclear Reactor Thermal
912 Hydraulics, Chicago, USA, August 30 – September 4.

913 Dabiri, S., Tryggvason, G., 2015. Heat transfer in turbulent bubbly flow in vertical channels. *Chem.*
914 *Eng. Sci.* 122, 106-113.

915 Daly, B.J., Harlow, F.H., 1970. Transport equations of turbulence. *Phys. Fluids* 13, 2634-2649.

916 Fox, R., 2012. Large-Eddy-Simulation tools for multiphase flows. *Annu. Rev. Fluid Mech.* 44, 47-
917 76.

918 Gosman, A.D., Lekakou, C., Politis, S., Issa, R.I., Looney, M.K., 1992. Multidimensional modeling
919 of turbulent two-phase flows in stirred vessels. *AIChE J.* 38, 1946-1956.

920 Grossetete, C., 1995. Experimental investigation and preliminary numerical simulations of void
921 profile development in a vertical cylindrical pipe. In: Serizawa, A., Fukano, T., Bataille, J.
922 (Eds.), 2nd International Conference on Multiphase Flow, Kyoto, Japan, April 3-7, IF1-1-10.

923 Hibiki, T., Ishii, M., 1999. Experimental study on interfacial area transport in bubbly two-phase
924 flows. *Int. J. Heat Mass Tran.* 42, 3019-3035.

925 Hibiki, T., Ishii, M., 2000. One-group interfacial area transport of bubbly flows in vertical round
926 tubes. *Int. J. Heat Mass Tran.* 43, 2711-2726.

927 Hibiki, T., Ishii, M., Xiao, Z., 2001. Axial interfacial area transport of vertical bubbly flows. *Int. J.*
928 *Heat Mass Tran.* 44, 1869-1888.

929 Hosokawa, S., Tomiyama, A., 2009. Multi-fluid simulation of turbulent bubbly pipe flow. *Chem.*
930 *Eng. Sci.* 64, 5308-5318.

931 Hulburt, H.M., Katz, S., 1964. Some problems in particle technology. *Chem. Eng. Sci.* 19, 555-574.

932 Ishii, M., Hibiki, T., 2006. *Thermo-fluid dynamics of two-phase flows.* Springer.

933 Jones, W.P., Launder, B.E., 1972. The prediction of laminarization with a two-equation model of
934 turbulence. *Int. J. Heat Mass Tran.* 15, 301-314.

- 935 Kataoka, I., Serizawa, A., 1989. Basic equations of turbulence in gas-liquid two-phase flow. *Int. J.*
936 *Multiphas. Flow* 15, 843-855.
- 937 Krepper, E., Lucas, D., Frank, T., Prasser, H.M., Zwart, P.J., 2008. The inhomogeneous MUSIG
938 model for the simulation of polydispersed flows. *Nucl. Eng. Des.* 238, 1690-1702.
- 939 Kumar, S., Ramkrishna, D., 1996. On the solution of population balance equations by discretization
940 –I. A fixed pivot technique. *Chem. Eng. Sci.* 51(8), 1311-1332.
- 941 Lahey Jr, R.T., Drew, D.A., 2001. The analysis of two-phase flow and heat transfer using a
942 multidimensional, four field, two-fluid model. *Nucl. Eng. Des.* 204, 29-44.
- 943 Lance, M., Bataille, J., 1991. Turbulence in the liquid phase of a uniform bubbly air-water flow. *J.*
944 *Fluid Mech.* 222, 95-118.
- 945 Lee, K., Matsoukas, T., 2000. Simultaneous coagulation and break-up using constant-*N* Monte
946 Carlo. *Powder Technol.* 110, 82-89.
- 947 Lehr, F., Millies, M., Mewes, D., 2002. Bubble-size distributions and flow fields in bubble
948 columns. *AIChE J.* 48(11), 2426-2441.
- 949 Liao, Y., Lucas, D., 2009. A literature review of theoretical models for drop and bubble breakup in
950 turbulent dispersions. *Chem. Eng. Sci.* 64, 3389-3406.
- 951 Liao, Y., Lucas, D., 2010. A literature review on mechanisms and models for the coalescence
952 process of fluid particles. *Chem. Eng. Sci.* 65, 2851-2864.
- 953 Liao, Y., Rzehak, R., Lucas, D., Krepper, E., 2015. Baseline closure model for dispersed bubbly
954 flow: bubble coalescence and breakup. *Chem. Eng. Sci.* 122, 336-349.
- 955 Lin, Y., Lee, K., Matsoukas, T., 2002. Solution of the population balance equation using constant-
956 number Monte Carlo. *Chem. Eng. Sci.* 57, 2241-2252.
- 957 Liu, T.J., 1993. Bubble size and entrance length effects on void development in a vertical channel.
958 *Int. J. Multiphas. Flow* 19(1), 99-113.
- 959 Liu, T.J., Bankoff, S.G., 1993. Structure of air-water bubbly flow in a vertical pipe – I. Liquid mean
960 velocity and turbulence measurements. *Int. J. Heat Mass Tran.* 36, 1049-1060.

961 Liu, T.J., 1998. The role of bubble size on liquid phase on liquid phase turbulent structure in two-
962 phase bubbly flows. Proceedings of the 3rd International Conference on Multiphase Flow, Lyon,
963 France, June 8-12.

964 Lo, S., 1996. Application of the MUSIG model to bubbly flows. AEAT-1096, AEA Technology.

965 Lo, S., Rao, P., 2007. Modelling of droplet breakup and coalescence in an oil-water pipeline. 6th
966 International Conference on Multiphase Flow, Leipzig, Germany, July 9-13, Paper 136.

967 Lo, S., Zhang, D., 2009. Modelling of break-up and coalescence in bubbly two-phase flows. J.
968 Comput. Multiphas. Flow 1, 23-38.

969 Lopez de Bertodano, M., Lahey Jr, R.T., Jones, O.C., 1994. Phase distribution in bubbly two-phase
970 flow in vertical ducts. Int. J. Multiphas. Flow 20, 805-818.

971 Lucas, D., Beyer, M., Szalinski, L., Schutz, P., 2010. A new database on the evolution of air-water
972 flows along a large vertical pipe. Int. J. Therm. Sci. 49, 664-674.

973 Lucas, D., Krepper, E., Prasser, H.M., 2005. Development of co-current air-water flow in a vertical
974 pipe. Int. J. Multiphas. Flow 31, 1304-1328.

975 Luo, H., Svendsen, H.F., 1996. Theoretical model for drop and bubble breakup in turbulent
976 dispersions. AIChE J. 42(5), 1225-1233.

977 Marchisio, D.L., Fox, R.O., 2005. Solution of population balance equations using the direct
978 quadrature method of moments. Aerosol Sci. 36, 43-73.

979 Marchisio, D.L., Fox, R.O., 2007. Multiphase reacting flows: modelling and simulation. Springer.

980 Molin, D., Marchioli, C., Soldati, A., 2012. Turbulence modulation and microbubble dynamics in
981 vertical channel flow. Int. J. Multiphas. Flow 42, 80-95.

982 Mukin R.V., 2014. Modeling of bubble coalescence and break-up in turbulent bubbly flow. Int. J.
983 Multiphas. Flow 62, 52-66.

984 Nandanwar, M.N., Kumar, S., 2008. A new discretization of space for the solution of multi-
985 dimensional population balance equations. Chem. Eng. Sci. 63, 2198-2210.

986 Nguyen, V.T., Song, C.H., Bae, B.U., Euh, D.J., 2013. Modeling of bubble coalescence and break-
987 up considering turbulent suppression phenomena in bubbly two-phase flow. *Int. J. Multiphas.*
988 *Flow* 54, 31-42.

989 Prasser, H.M., Beyer, M., Carl, H., Gregor, S., Lucas, D., Pietruske, H., Schutze, P., Weiss, F.P.,
990 2007. Evolution of the structure of a gas-liquid two-phase flow in a large vertical pipe. *Nucl.*
991 *Eng. Des.* 237, 1848-1861.

992 Prince, M.J., Blanch, H.W., 1990. Bubble coalescence and break-up in air-sparged bubble columns.
993 *AIChE J.* 36(10), 1485-1499.

994 Prosperetti, A., Tryggvason, G., 2009. *Computational methods for multiphase flow.* Cambridge
995 University Press.

996 Rzehak, R., Krepper, E., 2013. CFD modeling of bubble-induced turbulence. *Int. J. Multiphas.*
997 *Flow* 55, 138-155.

998 Santarelli, C., Roussel, J., Fröhlich, J., 2016. Budget analysis of the turbulent kinetic energy for
999 bubbly flow in a vertical channel. *Chem. Eng. Sci.* 141, 46-62.

1000 Sanyal, J., Vasquez, S., Roy, S., Dudukovic, M.P., 1999. Numerical simulation of gas-liquid
1001 dynamics in cylindrical bubble column reactors. *Chem. Eng. Sci.* 54, 5071-5083.

1002 Serizawa, A., Kataoka, I., Michiyoshi, I., 1975. Turbulence structure of air-water bubbly flow-II.
1003 Local properties. *Int. J. Multiphas. Flow* 2, 235-246.

1004 Shawkat, M.E., Ching, C.Y., Shoukri, M., 2007. On the liquid turbulence energy spectra in two-
1005 phase bubbly flow in a large diameter pipe. *Int. J. Multiphas. Flow* 33, 300-316.

1006 Smith, T.R., Schlegel, J.P., Hibiki, T., Ishii, M., 2012. Mechanistic modeling of interfacial area
1007 transport in large diameter pipes. *Int. J. Multiphas. Flow* 47, 1-16.

1008 Speziale, C.G., Sarkar, S., Gatski, T.B., 1991. Modelling the pressure-strain correlation of
1009 turbulence: An invariant dynamical system approach. *J. Fluid Mech.* 227, 245-272.

1010 Sun, X., Kim, S., Ishii, M., Beus, S.G., 2004. Modeling of bubble coalescence and disintegration in
1011 confined upward two-phase flow. *Nucl. Eng. Des.* 230, 3-26.

- 1012 Tomiyama, A., Tamai, H., Zun, I., Hosokawa, S., 1998. Transverse migration of single bubbles in
1013 simple shear flows. *Chem. Eng. Sci.* 57, 1849-1858.
- 1014 Tomiyama, A., Celata, G.P., Hosokawa, S., Yoshida, S., 2002a. Terminal velocity of single bubbles
1015 in surface tension dominant regime. *Int. J. Multiphas. Flow* 28, 1497-1519.
- 1016 Tomiyama, A., Tamai, H., Zun, I., Hosokawa, S., 2002b. Transverse migration of single bubbles in
1017 simple shear flows. *Chem. Eng. Sci.* 57, 1849-1858.
- 1018 Toutant, A., Labourasse, E., Lebaigue, O., Simonin, O., 2008. DNS of the interaction between a
1019 deformable buoyant bubble and a spatially decaying turbulence: A priori test for LES two-phase
1020 flow modelling. *Comput. Fluids* 37, 877-886.
- 1021 Troshko, A.A., Hassan, Y.A., 2001. A two-equation turbulence model of turbulent bubbly flows.
1022 *Int. J. Multiphas. Flow* 27, 1965-2000.
- 1023 Tryggvason, G., Buongiorno, J., 2010. The role of direct numerical simulations in validation and
1024 verification. *Computational Fluid Dynamics (CFD) for Nuclear Reactor Safety Applications*
1025 *OECD-NEA Workshop, Bethesda, USA September 14-16.*
- 1026 Ullrich, M., Maduta, R., Jakirlic, S., 2014. Turbulent bubbly flow in a vertical pipe computed by an
1027 eddy-resolving Reynolds stress model. 10th International ERCOFTAC Symposium on
1028 Engineering Turbulence Modelling and Measurements, Marbella, Spain, September 17-19.
- 1029 Vanni, M., 2000. Approximate population balance equations for aggregation-breakage processes.
1030 *J. Colloid Interf. Sci.* 221, 143-160.
- 1031 Wang, S.K., Lee, S.J., Jones Jr, O.C., Lahey Jr, R.T., 1987. 3-D turbulence structure and phase
1032 distribution measurements in bubbly two-phase flows. *Int. J. Multiphas. Flow* 13, 327-343.
- 1033 Wang, T., Wang, J., Jin, Y., 2005. Theoretical prediction of flow regime transition in bubble
1034 columns by the population balance model. *Chem. Eng. Sci.* 60, 6199-6209.
- 1035 Welleck, R.M., Agrawal, A.K., Skelland, A.H.P., 1966. Shape of liquid drops moving in liquid
1036 media. *AIChE J.* 12, 854-862.

- 1037 Wu, K., Kim, S., Ishii, M., Beus, S.G., 1998. One-group interfacial area transport in vertical bubbly
1038 flow. *Int. J. Heat Mass Tran.* 41, 1103-1112.
- 1039 Yao, W. and Morel, C., 2004. Volumetric interfacial area prediction in upward bubbly two-phase
1040 flow. *Int. J. Heat Mass Tran.* 47, 307-328.
- 1041 Yuan, C., Fox, R.O., 2011. Conditional quadrature method of moments for kinetic equations. *J.*
1042 *Comput. Phys.* 230, 8216-8246.
- 1043 Zhao, H., Maisels, A., Matsoukas, T., Zheng, C., 2007. Analysis of four Monte-Carlo methods for
1044 the solution of population balances in dispersed systems. *Powder Technol.* 173, 38-50.
- 1045
1046